

#### **PAPER • OPEN ACCESS**

# Linear and quasi-linear modeling in view of ELM control in MAST-U including effects of error fields

To cite this article: E. Tomasina et al 2025 Nucl. Fusion 65 106024

View the article online for updates and enhancements.

# You may also like

- Triangularity dependence of the divertor heat flux profile and SOL filamentary turbulence on TCV
- R.I. Morgan, G. Durr-Legoupil-Nicoud, O. Février et al.
- Orbit-space sensitivity of two-step reaction gamma-ray spectroscopy
   A. Valentini, H. Järleblad, M. Nocente et
- al.

   Excitation of toroidal Alfvén eigenmode by energetic particles in DTT and effect of
- Guangyu Wei, Fulvio Zonca, Matteo Valerio Falessi et al.



Nucl. Fusion 65 (2025) 106024 (20pp)

# Linear and quasi-linear modeling in view of ELM control in MAST-U including effects of error fields

E. Tomasina<sup>1,2,\*</sup>, M.J. Markl<sup>3</sup>, L. Pigatto<sup>2</sup>, D. Ryan<sup>4</sup>, A. Kirk<sup>4</sup>, C.G. Albert<sup>3</sup>, E. Viezzer<sup>5</sup>, Y.Q. Liu<sup>6</sup>, T. Bolzonella<sup>2</sup>, MAST-U Team<sup>a</sup> and the EUROfusion Tokamak Exploitation Team<sup>b</sup>

E-mail: edoardo.tomasina@igi.cnr.it

Received 14 April 2025, revised 26 July 2025 Accepted for publication 10 September 2025 Published 19 September 2025



#### **Abstract**

Edge localized modes (ELMs) pose a critical challenge to the safety and performance of plasma-facing components in tokamaks due to their periodic expulsion of heat and particles. This study investigates the behavior of various figures of merit for evaluating resonant magnetic perturbations (RMPs) as a tool for achieving ELM control in the spherical tokamak MAST-U. A combination of linear and quasi-linear modeling workflows, including MARS-F (single-fluid resistive MHD) and KilCA/QL-Balance (two-fluid kinetic) codes, was used to analyze plasma responses to RMPs under realistic operational conditions. To address recent experimental results, a detailed model for the n=2 intrinsic error field (EF) generated by the Poloidal Field coil system was developed, and the plasma response to this EF was computed. Results indicate that the n=2 EF is, at least, of the same order of magnitude as the perturbations introduced by the external RMP coils. In particular, the EF was found to significantly shift the optimal points of the analyzed metrics, affecting the effectiveness of ELM mitigation strategies and being detrimental to the core confinement when unfavorable aligned with the external RMPs, potentially explaining the observation of locked-modes. These results underscore the critical need for addressing intrinsic EF correction when designing ELM control strategies.

<sup>\*</sup> Author to whom any correspondence should be addressed.



Original Content from this work may be used under the terms of the Creative Commons Attribution 4.0 licence. Any

further distribution of this work must maintain attribution to the author(s) and the title of the work, journal citation and DOI.

<sup>&</sup>lt;sup>1</sup> Università degli Studi di Padova, Padova, Italy

<sup>&</sup>lt;sup>2</sup> Consorzio RFX (CNR, ENEA, INFN, Università di Padova, Acciaierie Venete SpA), Corso Stati Uniti 4, 35127 Padova, Italy

<sup>&</sup>lt;sup>3</sup> Fusion@OEAW, Graz University of Technology, Graz, Austria

<sup>&</sup>lt;sup>4</sup> UKAEA, Culham Campus, Abingdon OX14 3DB, United Kingdom of Great Britain and Northern Ireland

<sup>&</sup>lt;sup>5</sup> Department of Atomic, Molecular and Nuclear Physics, University of Seville, Spain

<sup>&</sup>lt;sup>6</sup> General Atomics, PO Box 85608, San Diego, CA 92186-5608, United States of America

<sup>&</sup>lt;sup>a</sup> See Harrison et al 2019 (https://doi.org/10.1088/1741-4326/ab121c) for the MAST-U Team.

b See Joffrin et al 2024 (https://doi.org/10.1088/1741-4326/ad2be4) for the EUROfusion Tokamak Exploitation Team.

Keywords: ELM control, resonant magnetic perturbations, error fields, plasma response, MHD modeling

(Some figures may appear in colour only in the online journal)

#### 1. Introduction

Edge localized modes (ELMs) are pressure-current driven hybrid MHD instabilities that periodically lead to the violent expulsion of heat and particles in a filamentary fashion when plasmas in tokamak configurations reach the so-called H-mode confinement [1]. In reactor-scale experiments such as ITER, controlling ELMs is crucial to ensure the safety of plasma-facing components, as the power deposited by ELM bursts scales with the size of the device [2]. Various techniques have been explored for ELM control, which can be broadly categorized into pacing, mitigation, and suppression strategies. ELM pacing is typically achieved through pellet injection [3], whereas mitigation and suppression are generally realized via the application of resonant magnetic perturbations (RMPs) through external, non-axisymmetric coils [4]. Mitigation refers to reducing the amplitude while increasing the frequency of ELM events [5, 6], whereas suppression describes a regime in which ELMs are completely eliminated [<del>7</del>].

Notably, ELM suppression has never been observed in tight aspect ratio, or spherical, tokamaks [8]. While ELM mitigation via RMPs was demonstrated in the earlier MAST experiment [9], replicating this success in MAST-U has proven challenging. Recent MAST-U campaigns have yielded mixed results, ranging from significant effects leading to mode-locking and disruptions to negligible impact [10]. Key differences between MAST-U and its predecessor include an increase in the maximum plasma current amplitude, accompanied by a reduction in the number of independently powered non-axisymmetric coils [11]. In particular, the previous coil set consisted in an upper row of six coils and a lower row of twelve. This allowed the achievement of a maximum of  $n_{\text{max}} = 3$  and  $n_{\text{max}} = 6$  respectively (with *n* being the discrete number denoting toroidal periodicity). Currently, in MAST-U the upper row has four coils (that is  $n_{\text{max}} = 2$ ) while the lower yields eight  $(n_{\text{max}} = 4)$ ; this reduction was necessary to accommodate the installation of the off-axis Neutral Beam Injector (NBI) and several diagnostics views. Moreover, the poloidal location of the new coils has been slightly tilted toward the midplane and the major radius position has been increased. While the coils for MAST-U have been constructed in the same way as the originals (54 cm  $\times$  22 cm square windows with four turns each), the power supplies feeding them have been updated, increasing the output current from 1.4 kA to 2kA (i.e from 5.6 kAt to 8 kAt). This, together with the new shaping capability of MAST-U which allows to bring the plasma boundary closer to the wall, allowed for reaching similar perturbed field magnitudes. A more quantitative comparison is reported in figure 2 in [10].

Moreover, so far RMP experiments have been conducted only in connected double null (CDN) discharges as no single null (SN) scenario was yet available. It is known that ELM control in CDN discharges is more challenging due to the reduced plasma response on the high field side (HFS) [12]. Since previous MAST experiments, modeling and empirical evidences have suggested the presence of a residual error field (EF) dominated by a n=2 component [10]. While in previous ELM control experiments the n=2 was less impacting because of the access to higher toroidal perturbations (see for ex: [5]), in the current state of the operations the EF could have a non-negligible impact. This could, in principle, explain the discrepancies between experimental results and predictions of the optimal phase alignment for achieving mitigation when operating with the RMP coils in n=2 configuration.

Expanding the modeling effort to understand these discrepancies, this work investigates the plasma response to external magnetic perturbations in MAST-U. The study evaluates and compares the roles of different metrics, both fluid and kinetic, while assessing the influence of kinetic parameters. Specifically, the magneto-hydrodynamic, resistive, linear code MARS-F [13] is applied to compute the perturbation field resulting from the combined effects of RMP coil currents and the plasma response. Classical fluid metrics derived from linear and quasi-linear response theories, are analyzed and re-evaluated by incorporating an EF model. Additionally, a quasi-linear figure of merit based on a kinetic plasma response model, computed within the KilCA framework [14] and previously applied to AUG results, is integrated into the analysis.

In the following: the numerical models used throughout the work are presented in section 2 and the different figures of merit applied are discussed in section 3. In section 4 the EF model is presented and its implications are discussed. Finally, section 5 includes the conclusions and the work summary.

#### 2. Modeling workflow

In this work, starting from the experimental discharges, a combination of numerical workflows has been implemented with the scope of deriving and comparing metrics for the optimization of RMPs in terms of ELM control. The summary of the complete process is summarized in figure 1. Results are mainly based on the application of the CHEASE/MARS-F workflow, where CHEASE is a well-established Grad-Shafranov solver [15] used to generate equilibrium inputs for subsequent plasma response calculations. The starting point for any plasma response evaluation is the equilibrium configuration, to which a perturbation can then be applied. To maintain consistency with experimental observations, the reconstructed equilibrium of an ELMy discharge from the MU-02 campaign has been chosen, specifically discharge #47051. A closely related discharge, #47052, was previously modeled with MARS-F to determine the optimal coil phasing

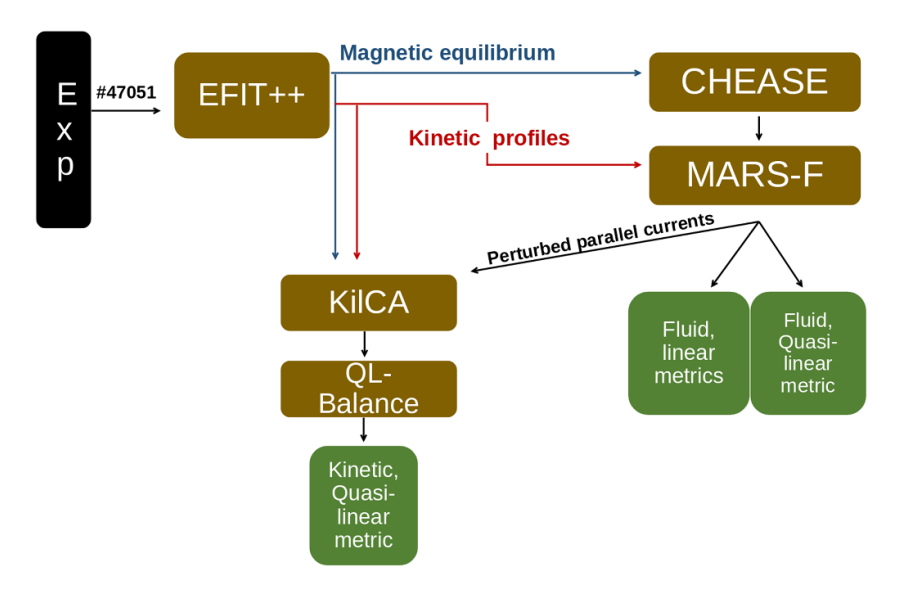
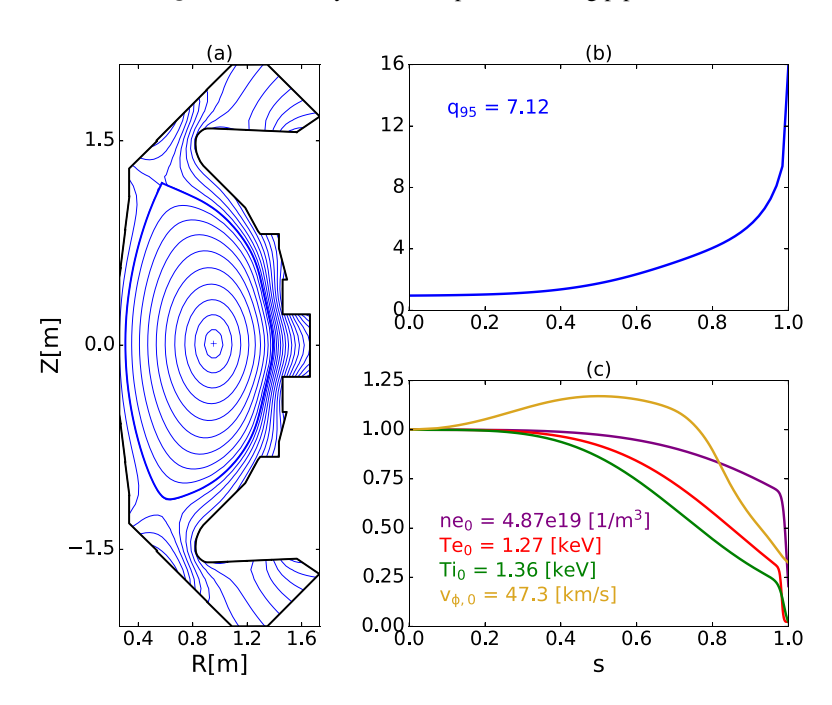


Figure 1. Summary of the complete modeling pipeline.



**Figure 2.** Equilibrium. *Left*: Magnetic flux reconstruction at 611 ms. *Right, top*: MSE constrained safety factor profile. *Right, bottom*: Kinetic profiles (EFIT++ reconstructed) provided as MARS-F inputs.

for ELM control experiments in the MU-03 campaign [10]. The equilibrium is prepared by running CHEASE on magnetically constrained data that has been processed with the EFIT++ [16] code. In MAST-U, equilibrium reconstructions are typically constrained using Motional Stark Effect (MSE) measurements [17], which provide a physical constraint on the internal current profile and thus on the safety factor (*q*) profile. Furthermore, to closely replicate experimental conditions, kinetic radial profiles are fitted within separate EFIT++ runs and provided to MARS-F as additional inputs. MAST-U diagnostics can reliably measure electron temperature and density, ion temperature and toroidal rotation velocity, though the latter two are only available when the diagnostic NBI is active.

Since MARS-F cannot explicitly handle the X-point singularity at the plasma boundary, a smoothing routine is applied in CHEASE before preparing inputs for plasma response computations. This smoothing reduces the edge safety factor  $(q_a)$  value but does not affect  $q_{95}$ , that is the value of q taken at the 95% of the poloidal flux. Previous studies have shown that that this kind of variations in  $q_a$  still yield similar plasma response spectra [18]. Figure 2 presents the equilibrium and kinetic profiles used for the MARS-F computations, where  $s = \sqrt{\frac{\psi - \psi_{\text{axis}}}{\psi_{\text{edge}} - \psi_{\text{axis}}}}$ , with  $\psi$  being the poloidal flux, is the normalized radial coordinate adopted in the code. It is important to note that, at this level, the kinetic profiles do not influence the equilibrium computation performed with CHEASE.

MARS-F solves the linearized MHD equations under the single-fluid, resistive approximation, within the resistiveinertial regime. These MHD equations account for a generic toroidal flow and couple with RMP source terms, modeled as an antenna problem. The system is expressed as follows:

$$i(\Omega_{\text{RMP}} + n\Omega)\boldsymbol{\xi} = \mathbf{v} + (\boldsymbol{\xi} \cdot \nabla\Omega)R\hat{\phi}$$
 (1)

$$i(\Omega_{\text{RMP}} + n\Omega) \mathbf{v} = -\nabla P + \mathbf{j} \times \mathbf{B} + \mathbf{J} \times \mathbf{b}$$

$$-\rho \left[ 2\Omega \hat{Z} \times \mathbf{v} + (\mathbf{v} \cdot \nabla \Omega_0) R \hat{\phi} \right]$$

$$-\rho k_{//} |\kappa_{//} v_{th,i}| \left( \mathbf{v} + (\boldsymbol{\xi} \cdot \nabla V_0) \right)_{//} \quad (2)$$

$$i(\Omega_{\text{RMP}} + n\Omega) \mathbf{b} = \nabla \times (\mathbf{v} + \mathbf{B}) + (\mathbf{b} \cdot \nabla \Omega) R \hat{\phi}$$

$$-\nabla \times (\eta \mathbf{j}) \quad (3)$$

$$i(\Omega_{\text{RMP}} + n\Omega)\mathbf{p} = -\mathbf{v} \cdot \nabla P - \Gamma P \nabla \cdot \mathbf{v}$$

$$+$$
(4)

$$\nabla \times \mathbf{b} = \mathbf{j}_{\text{RMP}}, \ \nabla \cdot \mathbf{j}_{\text{RMP}} = 0. \tag{5}$$

In this formulation, bold quantities represent 3D vectors, uppercase variables denote equilibrium quantities, and lowercase variables indicate perturbed quantities. The unit vector  $\phi$  points in the toroidal direction, while  $\hat{Z}$  indicates the vertical direction in the poloidal plane. For physical quantities, **J** represents the electric current, **B** the magnetic field,  $\xi$  the perturbed displacement,  $\mathbf{v}$  the perturbed velocity, P the pressure,  $\rho$  the plasma density, and  $\eta$  the resistivity. Additionally, R is the plasma major radius,  $\Omega$  is the toroidal rotation frequency, and thus  $V_0 = R\Omega \dot{\phi}$  is the toroidal, single-flow, velocity. The toroidal mode number is denoted as n, and  $\Gamma$  is the adiabatic index. The parallel wave number,  $\kappa_{//} = (n - \frac{m}{a})$  is defined using the poloidal mode number (m) and the safety factor q. Here,  $v_{th,i}$  represents the thermal ion velocity, and  $k_{//}$ is a numerical coefficient that mimics parallel sound damping [19]. In this study, a strong damping regime is assumed, corresponding to  $k_{//} = 1.5$ . The input RMP current,  $j_{RMP}$  is modeled as sinusoidal along the toroidal angle, with periodicity n, such that  $\mathbf{j}_{\mathbf{RMP}} \propto e^{in\phi}$ . Details of the implementation of the active coil currents in the code can be found in appendix of [20].

# 2.1. KilCA/QL-Balance kinetic model

External perturbations are usually effective in controlling ELMs only when they successfully penetrate into the plasma. As an initial response to external RMPs, parallel currents are built up in rational surfaces resonant to the applied perturbation field. These currents are oriented to produce a radial field opposite to the externally induced one in the attempt to reduce the perturbation, hence they are also referred to as *shielding currents*. The shielding to the external perturbation is proportional to the plasma flow. In principle, the parallel currents will interact with the radial field causing an electromagnetic torque which onsets a feedback loop that eventually may lead to the

flow braking and to the loss of shielding. The non-linear process for which the plasma response eventually fails in producing shielding is known as *bifurcation* [21]. Due to this cyclic nature of the RMPs dynamic, a quasi-linear model requires to be employed when studying penetration. In particular, within the fluid framework, perturbation penetration is assumed to be related to the bulk fluid braking exerted by the induced external fields. Alternatively, when considering the kinetic framework, the penetration is associated to the electron fluid braking.

Here, a quasi-linear kinetic response model has been applied to study penetration effectiveness with the KilCA/QL-Balance workflow. KilCA is a linear kinetic Maxwell equation solver in cylindrical geometry based on a finite Larmor radius expansion [14]. The equations that are solved in cylinder coordinates  $(r, \vartheta, z)$  are

$$\nabla \times \mathbf{E} - \frac{i\omega}{c}\mathbf{B} = 0, \quad \nabla \times \mathbf{B} + \frac{i\omega}{c}\mathbf{E} = \frac{4\pi}{c}(\mathbf{j} + \mathbf{j}_{\text{RMP}}). \quad (6)$$

Note the time-harmonic dependency and the use of CGS units. Also, due to the periodicity of the cylindrical model, a Fourier expansion in toroidal and poloidal angle can be employed. This casts the problem into a set of ordinary differential equations in the radial variable r. To connect the model to experimental profiles, the radial variable is set equal to an effective radius  $r \equiv r_{\rm eff} = \sqrt{2\psi_{\rm tor}/B_{\rm ref}}$ , where  $\psi_{\rm tor}$  is the toroidal flux and  $B_{\rm ref}$  is the reference magnetic field of the equilibrium at the magnetic axis. The experimental profiles given as a function of the square root of the normalized poloidal flux are mapped to  $r_{\rm eff}$ .

The current density in Ampere's law in (6) is given by two parts: the RMP current density provided by an antenna (i.e. the active coil) outside the plasma  $j_{RMP}$  and the plasma response current j. The plasma response current is determined in kinetic theory with a finite Larmor radius expansion to order  $N_{FLR}$  as

$$j_{mn}^{i}(r) = \frac{1}{r} \sum_{k,k'=0}^{N_{\text{FLR}}} (-1)^{k} \frac{\partial^{k}}{\partial r^{k}} \left( r \sigma_{kk',mn}^{il}(r) \frac{\partial^{k'}}{\partial r^{k'}} E_{mnl}(r) \right), \quad (7)$$

where the apex i identifies the spatial components and the species index is suppressed here for brevity. The current is determined for a specific poloidal and toroidal mode number m and n, respectively, by the conductivity tensor  $\sigma$ . The conductivity tensor is derived from the solution to the kinetic equation with a Fokker–Planck type collision operator in the Ornstein–Uhlenbeck approximation including an energy-preserving integral term. For more details see [14, 22]. In the following,  $N_{\rm FLR} = 1$  is used.

QL-Balance [14] is a quasi-linear 1D radial transport code which takes inputs from the linear kinetic response. This model solves transport equations for the electron density, electron and ion temperature, and the toroidal rotation velocity based on drift-kinetic transport coefficients  $D^{q1}$  that are determined by the electromagnetic field perturbations of KilCA. The radial electric field is determined via the ion force balance, where the poloidal rotation is calculated by the drift-kinetic solver NEO-2 [14, 23].

Furthermore, anomalous transport is taken into account by a diffusion coefficient  $D^a$ . Without any prior knowledge of the anomalous heat diffusion coefficient, its value can be approximated according to the following procedure. Starting by assuming a cylindrical plasma with a single ion species and  $T_e = T_i$ , the energy confinement time  $\tau_E = W/P$  is given by the ratio of the total stored energy  $W = \pi R_0 \int_0^a dr \ r 3n_e T_e$ and the input power  $P = \pi R_0 \int_0^a dr \, r \mathcal{P}$  where  $\mathcal{P}$  is the input power density, and  $a(R_0)$  is the plasma minor (major) radius. Also, for simplicity, P and  $n_e$  are assumed constant here. Considering the steady-state heat transport equation and the equipartition of the input power to both species, the temperature can be derived to be  $T_e(r) = (a^2 - r^2)\mathcal{P}/(8n_eD^a)$ , where  $D^{a}$  is the anomalous heat diffusion coefficient which is also assumed constant. Here, the boundary conditions  $\partial_r T_e|_{r=0} = 0$ and  $T_e(a) = 0$  have been employed. Using  $T_e(r)$  in the definition of the energy confinement time and performing the integral, one obtains:

$$D^{a} = \frac{3a^2}{32\tau_E}. (8$$

For typical MAST parameters [24], that is a = 0.56 m and  $\tau_E = 0.0034$  s, this estimate turns out to be  $D^a = 0.87$  m<sup>2</sup> s<sup>-1</sup>, which in this work has been eventually set to  $D^a = 1$  m<sup>2</sup> s<sup>-1</sup>. This value was also used in earlier studies of ASDEX Upgrade [14, 25].

2.1.1. Toroidal rescaling. A drawback of the cylinder model is the lack of poloidal mode coupling which can significantly affect the magnitude of the shielding [26]. This issue was addressed already for the modeling of ASDEX-Upgrade in [14] by rescaling the electromagnetic fields calculated by KilCA with a scaling factor

$$C_{mn} = \frac{I_{\parallel,mn}^{\text{tMHD}}}{I_{\parallel,mn}^{\text{KilCA}}},\tag{9}$$

given by the integrated parallel shielding currents determined by a chosen toroidal MHD code  $(I_{\parallel,mn}^{\text{tMHD}})$  and by KilCA  $(I_{\parallel mn}^{\text{KilCA}})$ . In previous work studying ASDEX-Upgrade, the toroidal ideal MHD code GPEC [27, 28] was used. Here, the toroidal shielding current is provided by MARS-F. The computation of the parallel current in MARS-F and its integration into the KilCA current are summarized in appendix, the latter part is also exhaustively described in [14]. The rescaling is motivated by the similarities between the plasma response in the fluid and kinetic models in the case of strong shielding. Although single-fluid theory does not capture electron dynamics, the total shielding current is only weakly sensitive to the details of the current density. Therefore, as long as strong shielding persists, the toroidal rescaling remains valid. Once the shielding weakens, the system enters a nonlinear regime where the linear codes are formally no longer applicable anyway. For more details, see reference [14].

#### 3. Metrics

When preparing an ELM control experiment, the routine procedure involves running a linear MHD code, such as GPEC or MARS-F, to quickly predict the coil phasing that optimizes a specific objective function or metric. In MAST and ASDEX [6], successful experiments have been conducted by maximizing the magnitude of the radial component of the edge-resonant perturbation field,  $b_{\text{edge,res}}^1$ , which is nominally defined as:  $\frac{\mathbf{b} \cdot \nabla \psi}{\mathbf{B}_0 \cdot \nabla \phi} \frac{q}{R_0^2 B_0}$ . Here  $\psi$  and  $\phi$  are respectively the poloidal and toroidal fluxes,  $R_0$  is the machine axis position and  $B_0$  is the equilibrium magnetic field at the axis. This quantity is calculated in straight field line (SFL) coordinates, or PEST-like, within MARS-F and serves as a figure of merit for quantifying the perturbation effectively injected into the edge plasma, accounting for the plasma response. The subscript 'edge, res' identifies one or more Fourier harmonics which resonate with the respective rational surfaces located in the edge region of the plasma. Historically, and in many works, the last pitch aligned surface is chosen [10, 29], while this is the most convenient choice for the purpose of comparing with magnetic data, the last resonant surface may be potentially ill defined as it depends on equilibrium reconstruction and on the smoothing procedure. For this reason some authors prefer to investigate the plasma response at the pedestal [6] or at the pedestal top regions [30]. By looking at figure 3, the positions of these three resonant surfaces can be identified. Specifically, the resonant surfaces at the pedestal top, the steep gradient region and the last pitch-aligned can be respectively identified by the poloidal mode numbers: m = 7, 9, 11 for the n = 1 and by m = 14, 19, 22 for the n = 2. The resonant field metric is particularly valuable for coil systems that may struggle to surpass the threshold field or input current required to achieve ELM mitigation. It is especially useful for higher n perturbations, which tend to penetrate less effectively due to the higher number of rational surfaces concentrated in the edge and to a faster spatial decay. At lower n and for sufficiently powerful coil systems, the injected perturbation may trigger a locked mode (LM) [21], potentially leading to plasma termination. In such cases, a figure of merit that decouples the effects of the perturbation at the edge and core is preferred. The objective is to degrade the edge confinement just enough to stabilize the ELM while preserving favorable conditions in the plasma core [31]. To this end, metrics such as  $\xi_X^N/\xi_{\text{mid}}^N$  or  $au_{
m edge}/ au_{
m core}$  are often maximized. The first metric,  $\xi_X^N/\xi_{
m mid}^N$ , represents the ratio of the normalized plasma displacement at the X-point to that at the mid-plane. This is considered a robust marker of confinement degradation induced by the application of RMPs. Studies have shown that the X-point displacement tends to couple strongly with a peeling-like plasma response, which is closely associated with edge stability, whereas midplane displacement is typically linked to a kink-like response that penetrates further into the plasma core [29]. This behavior has been corroborated by ELM mitigation experiments conducted in ASDEX and MAST [6]. Notice that, since in MARS-F the X-points are not reproduced, the  $\xi_X^N$  displacements are computed by averaging the regions around the upper

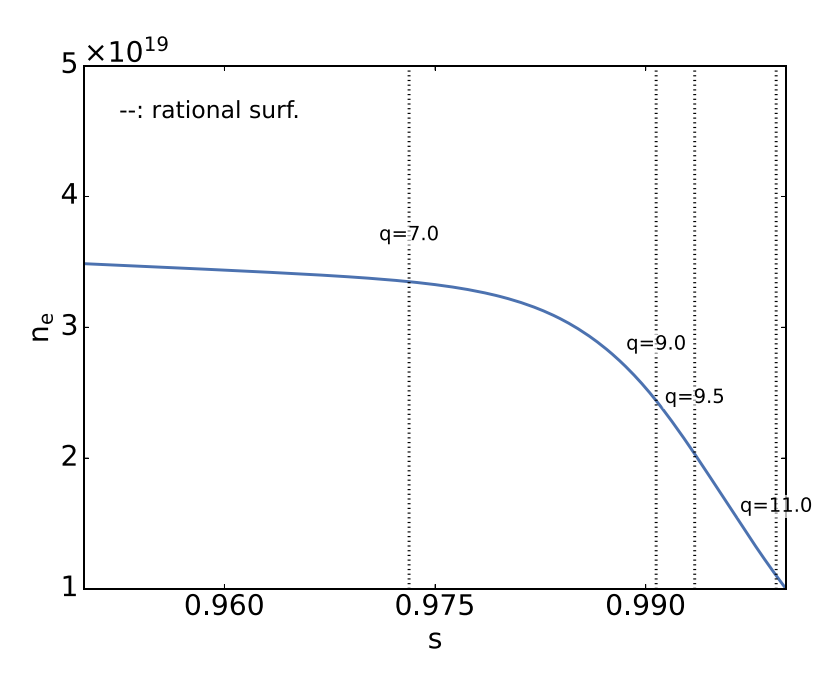


**Figure 3.** Zoom-in of the density profile around the pedestal region. A few of the rational surfaces relevant for this study have been highlighted with dotted lines.

most and lower most points of the boundary. The second metric,  $\tau_{\rm edge}/\tau_{\rm core}$  corresponds to the ratio of the integrated total torque injected, by the RMPs, into the edge region to that injected in the core region. This metric provides a complementary view for evaluating the effects of RMPs on edge and core dynamics [32].

## Linear metrics

MARS-F operates within the linear physics framework, meaning that the superposition of computed solutions also constitutes valid solutions. Mathematically, if *X* is a generic solution, the expression  $X_{\text{tot}} = A \cdot X_L + B \cdot X_U e^{i\Delta\phi}$  remains a solution in MARS-F. Here, A and B are arbitrary coefficients, and  $\Delta \phi$  represents the relative toroidal variation between the coil rows. As introduced above, MAST-U is currently equipped with 2 rows of ELM coils. Such coils are placed in-vessel on the the Low Field Side, covering the whole toroidal angle. Of course, since the two rows have a different number of identical coils, also the spacing between each of them is different among the row. In this work the relative phase between respective coils at the same toroidal position is defined as  $\phi_{\mathrm{UPPER}} - \phi_{\mathrm{LOWER}},$  that is: the upper coil row is treated as fixed at  $\phi_{\text{UPPER}} = 0^{\circ}$ , while the lower coil row, which has a greater number of degrees of freedom, is varied clockwise. This property enables a rapid exploration of all possible coil-set combinations in terms of input current amplitude and toroidal phasing. Such efficiency is leveraged to identify optimal configurations for addressing the ELM mitigation or suppression problem by analyzing the behavior of various (linear) output quantities while scanning the parameter space of the input currents. The optimization results for the first two metrics, assuming an input current of 1 kAt, are illustrated in figure 4 for the two toroidal mode numbers, n = 1 and n = 2. The computed optimal phasing values for each metric align well with those reported in [10]. As anticipated, the optimal phase is sensitive to the applied toroidal mode number but exhibits similar trends in both cases. Notably, the plasma response always introduces a shift of the optimal phase, of  $\sim 60^{\circ}$  for the n=1 and of  $\sim 40^{\circ}$ for the n = 2, with a dependence of few degrees on the poloidal mode number. The only exception to this trend appears in the field computed at the outermost surface for the n=1case (red circles, top left plot of figure 4). Here, including the plasma response leads to an optimal value shifted by  $\sim 90^{\circ}$ , with a magnitude lower than that at inner surfaces, indicating exceptionally strong shielding. This behavior is not observed at the outermost surface resonant with the n = 2 perturbations (red circles, top right plot of figure 4) which behaves more regularly. Additionally, the displacement metric achieves optimization at nearly the same relative phase when considering the displacement at both the lower and upper X-points. Strictly in terms of magnitudes, the displacement at the upper X-point exceeds that at the lower X-point for both the n = 1 and n = 2cases, measuring  $\xi_U = 0.49 \text{ mm kAt}^{-1}$ ,  $\xi_L = 0.3 \text{ mm kAt}^{-1}$ and  $\xi_U = 0.39 \text{ mm kAt}^{-1}$ ,  $\xi_L = 0.18 \text{ mm kAt}^{-1}$  respectively.

#### Quasi-linear fluid metric

The torque induced by externally generated 3D fields is inherently a non-linear effect, as it depends quadratically on the perturbation. In MARS-F, various types of physical torques can be calculated based on the plasma response results. Specifically, the electromagnetic  $(\mathbf{j} \times \mathbf{b})$ , neoclassical toroidal viscosity (NTV), and Reynolds stress (REY) torque sources are included in this work. The  $\mathbf{j} \times \mathbf{b}$  and REY torques are purely MHD-driven, with the former originated by the interaction between the perturbed field  $(b^1)$  and the shielding currents built in response to it  $(j^2)$  and the latter associated to the

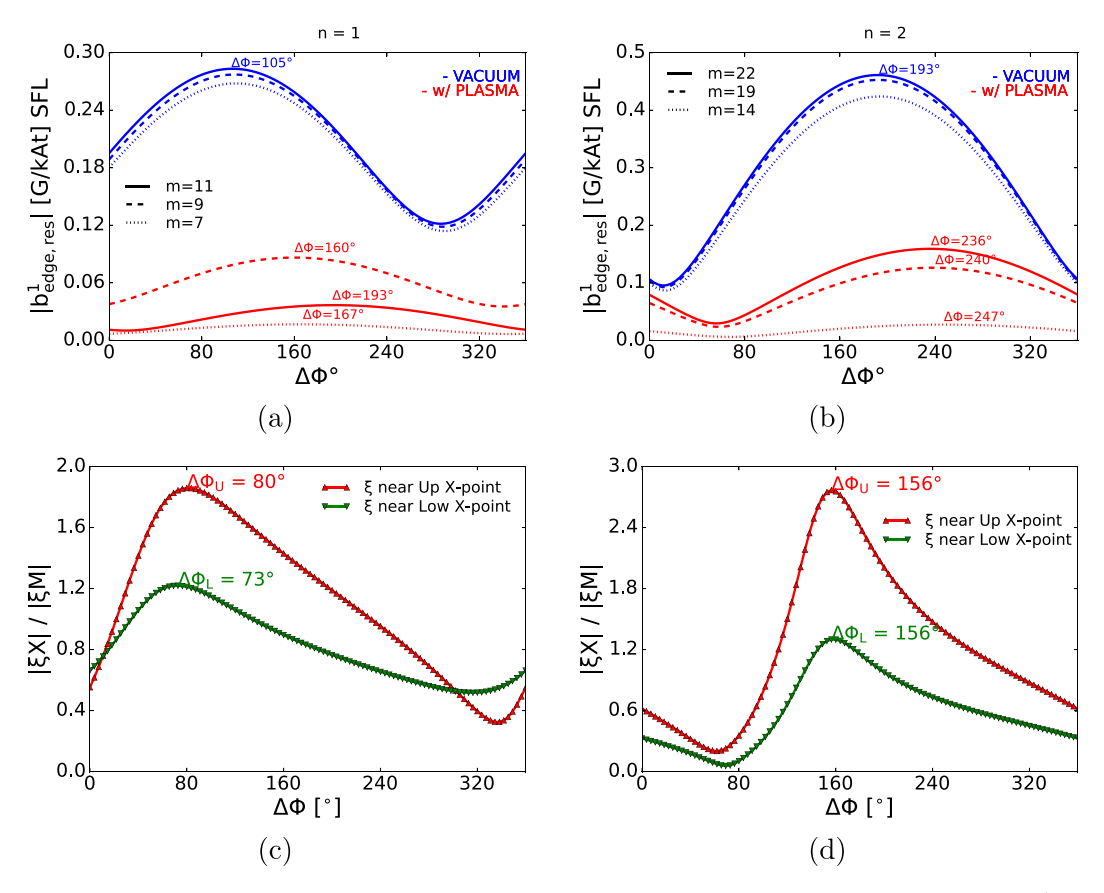


**Figure 4.** Fluid linear metrics dependence on relative coil phase  $\Delta \phi$ . (a) and (c): n = 1, (b) and (d): n = 2. (a) and (b):  $|b_{\text{edge,res}}^1|$  metric (renormalized to physical units) for different poloidal mode numbers, with blue: vacuum only and red: vacuum + plasma response. (c) and (d):  $\xi_{\text{X-point}}^N/\xi_{\text{mid-plane}}^N$  metric, with red:  $\xi_{\text{upperX-point}}^N$  and green:  $\xi_{\text{lowerX-point}}^N$ .

REY tensor term, that is  $\propto (\mathbf{v} \cdot \nabla) \mathbf{v}$ . A comprehensive evaluation of the NTV torque, instead, would require a full kinetic or drift-kinetic treatment. However, in MARS-F, an analytic formula is implemented to bridge different collisionality regimes, as detailed in [33, 34]. Comparisons of this NTV computation with kinetic treatments have demonstrated qualitative agreement [35]. To leverage the linearity advantages of the framework, some manipulation of the torque outputs is necessary. For this purpose, a semi-analytic algorithm is integrated into the code to construct a torque matrix that incorporates terms accounting for mutual coupling between the rows of coils [36]. This approach generalizes the torque computation for arbitrary input current values  $\mathbf{I}$ , as described by the following relationship:

$$\Pi^{\alpha}(s) = \mathbf{I} \cdot \mathbf{\Pi}_{\mathbf{M}}^{\alpha}(s) \cdot \mathbf{I}^{*} = \begin{bmatrix} I_{U} & I_{L} \end{bmatrix} \begin{bmatrix} \Pi_{UU}^{\alpha} & \Pi_{UL}^{\alpha} \\ \Pi_{LU}^{\alpha} & \Pi_{LL}^{\alpha} \end{bmatrix} (s) \begin{bmatrix} I_{U}^{*} \\ I_{L}^{*} \end{bmatrix}$$
(1)

where  $\Pi^{\alpha}(s)$  is the surface-averaged torque density and  $\alpha = \mathbf{j} \times \mathbf{b}$ , NTV, REY. The superscript \* denotes the complex-conjugate of the vector.

In order to maximize the  $\tau_{\rm edge}/\tau_{\rm core}$  ratio, we first define  $\Pi^{\rm tot} \equiv \sum_{\alpha} \Pi^{\alpha}$  and then take the radial integral separating the

core and edge regions:

$$\tau_{\rm core} \equiv \int_0^{0.89} \Pi^{\rm tot}(s) \, \mathrm{d}s \tag{11}$$

$$\tau_{\text{edge}} \equiv \int_{0.89}^{1} \Pi^{\text{tot}}(s) \, \mathrm{d}s \tag{12}$$

where the boundary among the two regions has been set s = 0.89. Of course the separation between the two regions retains a degree of freedom, however, as long as the edge region contains the pedestal, the results are fairly robust to variation of this parameter [32]. In figure 5, a scan in input current for determining the total integrated torque is reported for both toroidal mode numbers n = 1 and n = 2 and for both the edge and the core regions. In the scan the upper row of coils is again considered fixed while the lower row is allowed to vary between  $[0-360]^{\circ}$ . For both rows the input current is also scanned in amplitude, ranging between [1-8] kAt. Notice that the maximum current achievable in MAST-U active coils consists of a total of 8 kAt. For both cases, the core minimization and the edge torque maximization are generally located at different phases. The result of the torque ratio optimization is shown in figure 6. Here, another free parameter for the coil set configuration has been introduced in the form of the current amplitude ratio  $I_L/I_U$ . This parameter was varied to

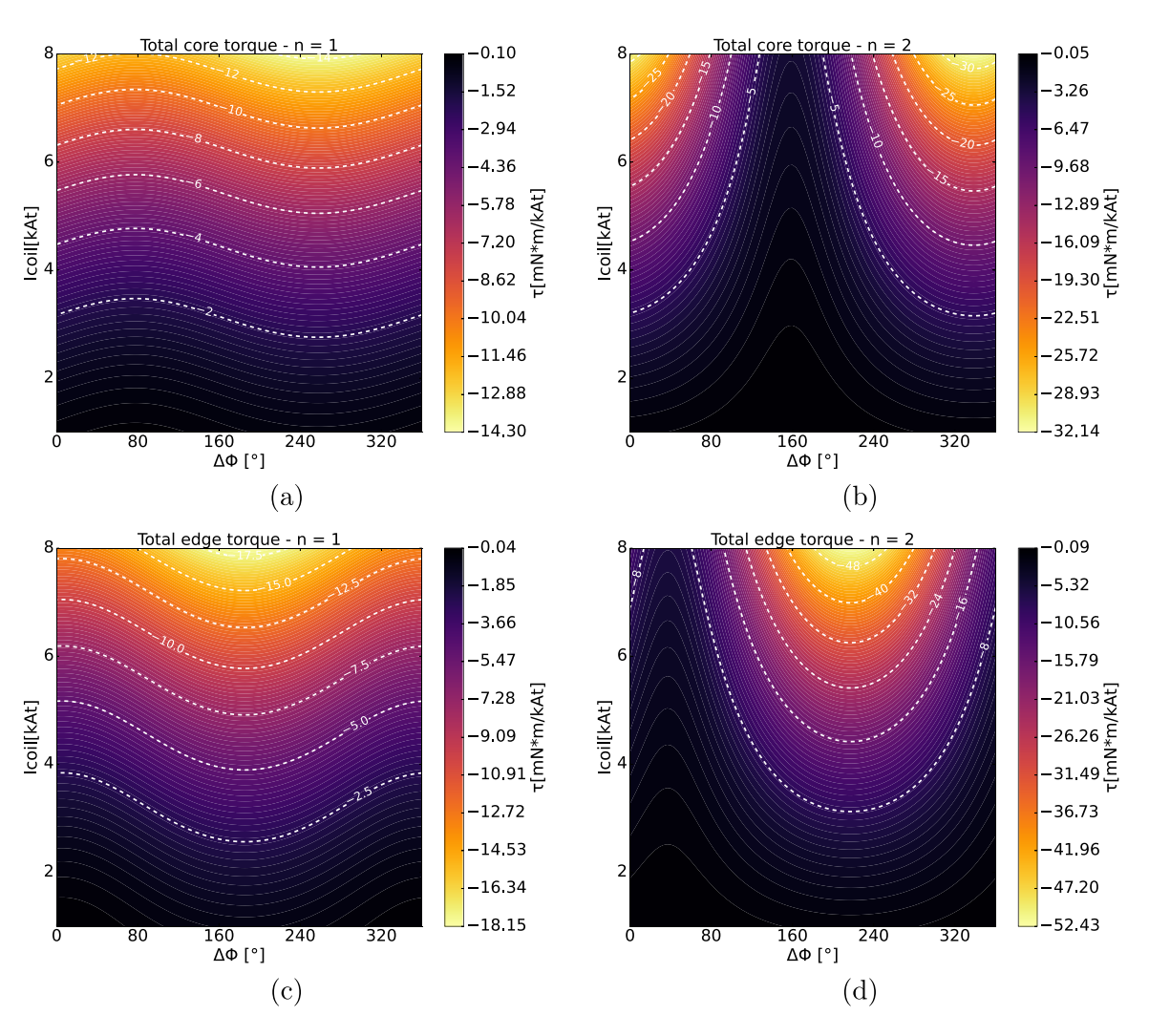


**Figure 5.** Integrated total torque obtained by varying the current magnitude and relative phase between the upper and lower coilsets. (a) n = 1, core region, (b) n = 2, core region. (c) n = 1, edge region. (d) n = 2, edge region.

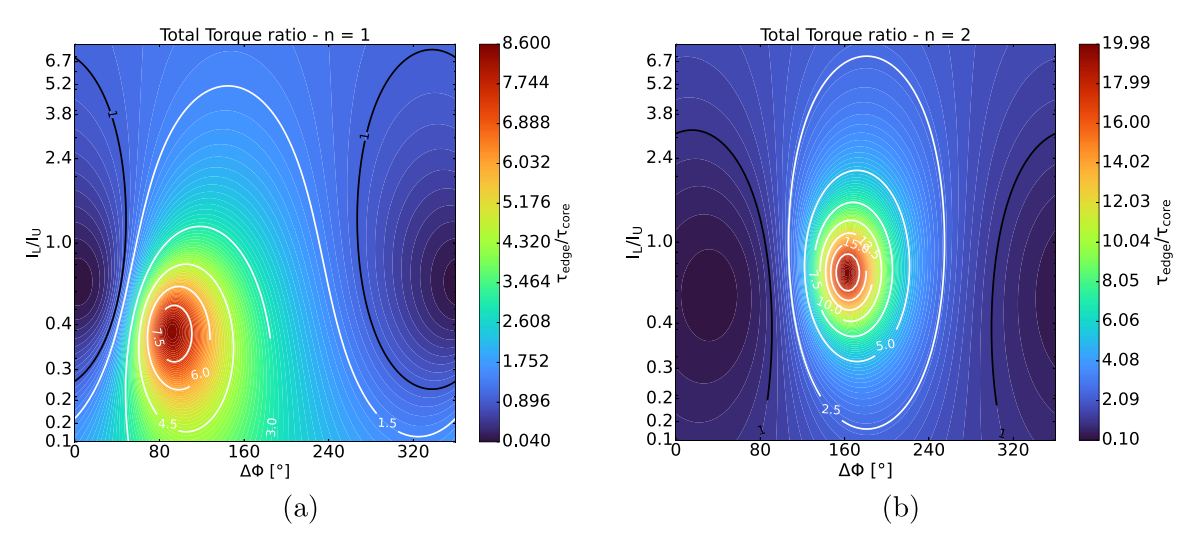


**Figure 6.** Torque ratio,  $\tau_{\rm edge}/\tau_{\rm core}$ , varying the current amplitude ratio  $I_L/I_U$  and  $\Delta\phi$  for n=1 (a) and n=2 (b) configurations. The black solid contour highlights where the ratio is =1.

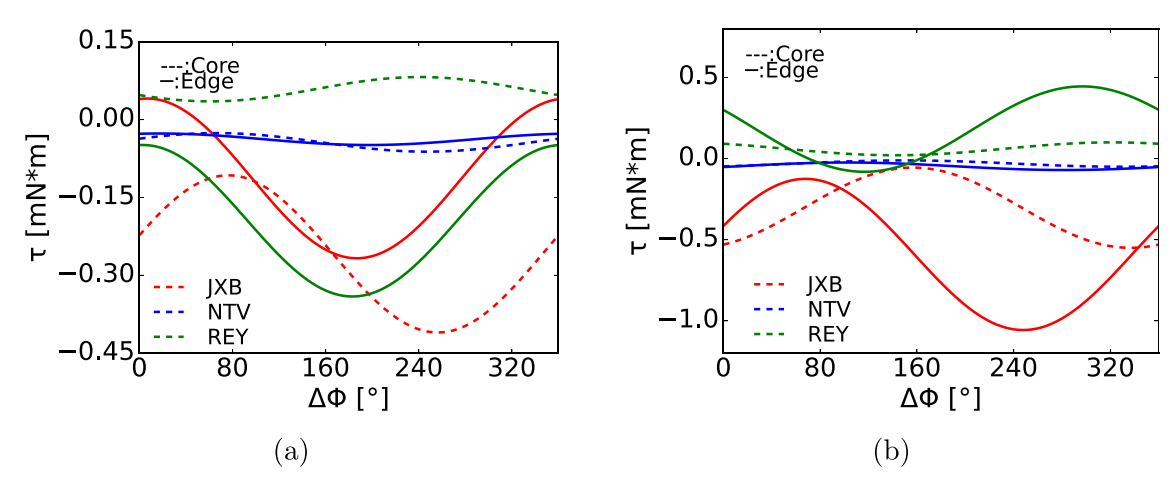


Figure 7. Integral torques split by source and region. Assuming  $I_U = I_L = 1$  kAt. (a) n = 1, (b) n = 2. Solid lines corresponds to the edge while dashed lines identify the core. A color code is used to distinct each torque source, so red:  $\mathbf{j} \times \mathbf{b}$ , blue: NTV and green: REY.

assess the relative coupling strength of each row to the core and edge regions of the plasma independently. Notably, this metric shows strong agreement with the displacement ratio metric in terms of optimal phase, with the maximum edge-to-core torque ratio occurring at a relative phase of  $\Delta\phi \sim 80^\circ$  for the n=1 and  $\Delta\phi \sim 160^\circ$  for the n=2. Moreover, figure 6 suggest that the maximum ratio would be obtained with a current amplitude ratio  $I_L/I_U \sim 0.7$  for the n=2 and  $I_L/I_U \sim 0.35$  for the n=1. Interestingly, the torque ratio could remain above the unity for any value of  $\Delta\phi$  when  $I_L/I_U < 0.3$  for the n=1 and  $I_L/I_U > 3$  for the n=2 case.

It is possible to analyze more in detail each source of torque, in each spatial region, at the variation of  $\Delta \Phi$ . This is shown in figure 7 for both the n=1 and the n=2 mode numbers.

Focusing first on the n=1 component, within the core region (dashed line in the figure) it appears that the REY and  $\mathbf{j} \times \mathbf{b}$  torques are in competition, with the latter being bigger hence driving the global flow braking. Moving in the edge region the picture changes, for most of the  $\Delta \Phi$  values  $\mathbf{j} \times \mathbf{b}$ and REY torques are aligned in braking the flow. The optimum of the torque ratio metric is justified by observing that, while in the edge the braking is strongly amplified at  $\Delta\Phi \sim 180^{\circ}$ , in the core the integral  $\mathbf{j} \times \mathbf{b}$  torque has a minimum, whereas the REY torque is only slightly varying. As a consequence, around  $\Delta\Phi\sim80^\circ$  the sum of the two components approaches the zero favoring the satisfaction of the core torque minimization requirement. For the n = 2 case the picture is similar even if with some differences, now in the edge region (solid lines, left panel of figure 7) REY and  $\mathbf{j} \times \mathbf{b}$  are almost always in competition with the viscous term trying to compensate the electromagnetic-induced braking. The core torque is smaller than the edge one in the majority of the relative phase space. In particular, its  $\mathbf{j} \times \mathbf{b}$  component is minimal in the correspondence of the zero of the REY-driven edge acceleration, which is located at  $\Delta\Phi \sim 160^{\circ}$ , this allows to simultaneously achieve both the edge and core torque requirements. Finally, the NTV contribution to the total toroidal torque is always at least one order of magnitude less than the others. Therefore evolution of the velocity profile can be interpreted as being predominantly driven by the competition between the electromagnetic braking (induced by the external coils) and the correspondent inertial viscous drag of the plasma.

#### Quasi-linear kinetic metric

To determine the actual effectiveness of the perturbations achieved with the MAST-U ELM coil system, the KilCA/QL-Balance quasi-linear framework has been implemented. Within the framework a criterion for the bifurcation of an arbitrary mode was defined in [14]. This criterion is characterized by a ratio of diffusion coefficients,

$$D_{mn} \equiv \frac{D_{e,22}^{q1}}{D^{a}} \bigg|_{q=0} \ge 1. \tag{13}$$

Here,  $D_{e,22}^{q1}$  is the quasi-linear electron heat diffusion coefficient determined within drift-kinetic theory employing a Fokker–Planck collision operator in the Ornstein–Uhlenbeck approximation. For the expression of the quasi-linear diffusion coefficient see reference [14].  $D^a$  is the anomalous diffusion coefficient, which is set to 1 m<sup>2</sup> s<sup>-1</sup>. The criterion is based on the observation that a feedback loop enabling bifurcation, by local rotation braking or acceleration to approach the electron fluid resonance, is triggered when the quasi-linear diffusion increases to the size of the anomalous one. The diffusion ratio is evaluated at the effective radius  $r_{mn}$  of the resonant surface. Since mode penetration of a resonant surface on the pedestal top is commonly assumed to be a requirement for ELM suppression [37], the focus of this metric are modes located near the pedestal top.

In this work, the criterion (13) as a metric for ELM control is applied. In particular, when scanning over the differential phase  $\Delta \Phi$ , the maximum of  $D_{mn}$  indicates the optimal coil configuration for mode penetration while the value assumed by the ratio suggests its actual effectiveness.

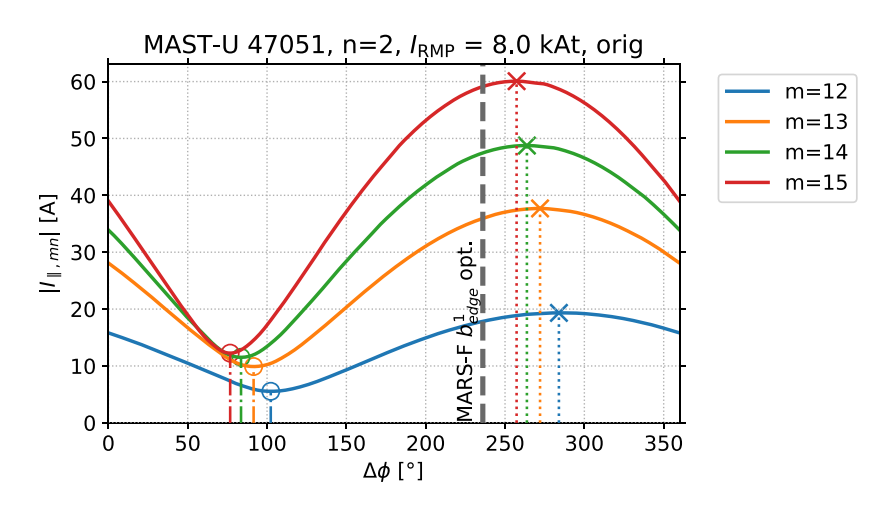


**Figure 8.** Integrated MARS-F current. The harmonics are given for Boozer angles. The maximum tends toward the optimum of the MARS-F metric  $b_{\text{edge,res}}^1$  (vertical dashed line) for higher mode numbers.

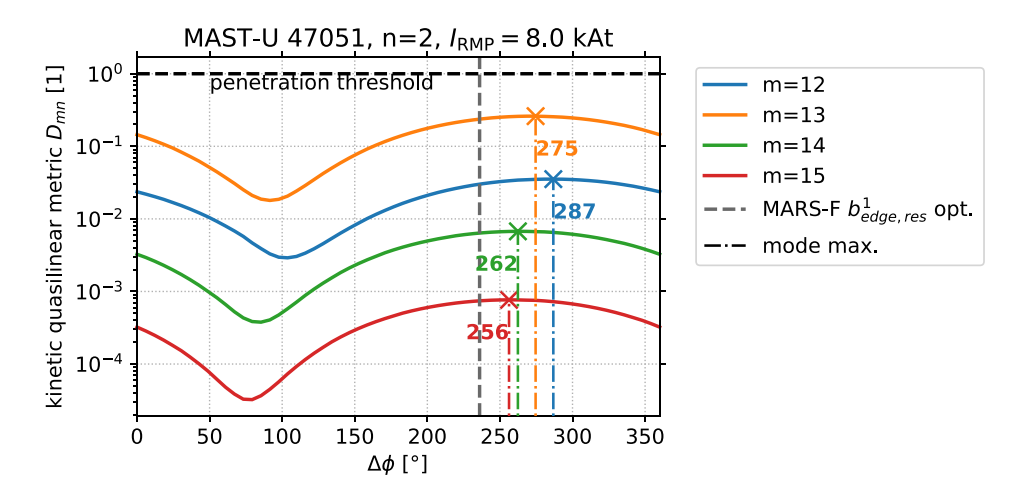


Figure 9. Kinetic quasi-linear metric for the n = 2 perturbation. The maximum predicted by MARS-F is, again, highlighted by the vertical, dashed line.

A first qualitative assessment can be provided by the analytic expression of the quasi-linear diffusion coefficient in constant- $\psi$  approximation given by equation (51) in [14]. The expression shows that the coefficient is proportional to the parallel shielding current squared,  $D_{e,22}^{q1} \propto |I_{\parallel}|^2$ . This statement is independent on the model in which the current is calculated. Hence, since the  $\Delta\Phi$  toroidal dependence can only be introduced from MARS-F results, assuming constant anomalous diffusion, the optimum of the kinetic metric  $D_{mn}$  has to coincide with the maximum of the shielding currents. Figure 8 shows the integrated current for MAST-U n = 2 perturbations for various poloidal mode numbers m that are near the pedestal top. These are calculated as described in appendix. The values are given for the maximum RMP coil current possible in MAST-U ( $I_{RMP} = 8 \text{ kAt}$ ). The maxima of the shielding current indicated by 'x' markers simultaneously indicate the optimal differential phase to achieve bifurcation of the respective mode. The optimal differential phase for the edge modes is, within a few degrees, in agreement with the prediction of the linear fluid metric  $b_{\text{edge,res}}^1$ , as shown in figure 4.

On the other hand, core modes, which should ideally not penetrate, have maxima and minima at higher differential phase values compared to the edge modes. As discussed above, for achieving ELM mitigation/suppression, it is desirable to minimize the core response, while maximizing the edge response. Hence, the optimal differential phase for the experiment lies within the minimum of the core modes and the maximum of the edge modes. This first assessment indicates the differential phase for optimal edge response, but it does not infer on actual mode penetration. For this, the kinetic metric with KilCA/QL-Balance is calculated (including the toroidal rescaling described in section 2.1.1). Figure 9 shows the kinetic metric for various poloidal mode numbers located near the pedestal top for n = 2. Indicated by dashed–dotted lines are the maxima of each mode. Notably, the magnitude of the metric does not imply the bifurcation of any of the modes.

In terms of optimal differential phase, the trend of  $D_{mn}$  goes toward the optimal value of  $b_{\text{edge,res}}^1$  for higher poloidal mode numbers. The jump between optimal phases across rational surfaces is larger than that seen with the linear resonant field metric. Specifically, near the pedestal top (m = 14, 15) the

quasi-linear criterion predicts an optimal phase about  $\sim 20^{\circ}$ higher than the linear one. However, this is well within the broadness of the peak. The cylindrical model of KilCA is not valid anymore at the outermost edge of the plasma where the model's neoclassical reconstruction of the radial electric field loses validity. In fact, the kinetic criterion is mostly reliable (and hence it should be used) when considering the optimization around the pedestal top [14]. The fluid and the kinetic metric can be compared in such region only in terms of optimal differential phase, as the quantification of the magnitude of the resonant perturbed field within any inner resonant surface is complicated by the presence of a strong shielding. Therefore, the fluid metric can quantitatively inform only for regions closer to the separatrix, that is m = 22 for  $q_{\text{edge}} = 11$ and n = 2 for the case at hand. As a result, KilCA/QL-Balance computations provide a more reliable pedestal-located penetration criterion which could be in principle a more effective predictor of RMP induced ELM control, than the conventional linear fluid based metrics.

# 4. Error field (EF)

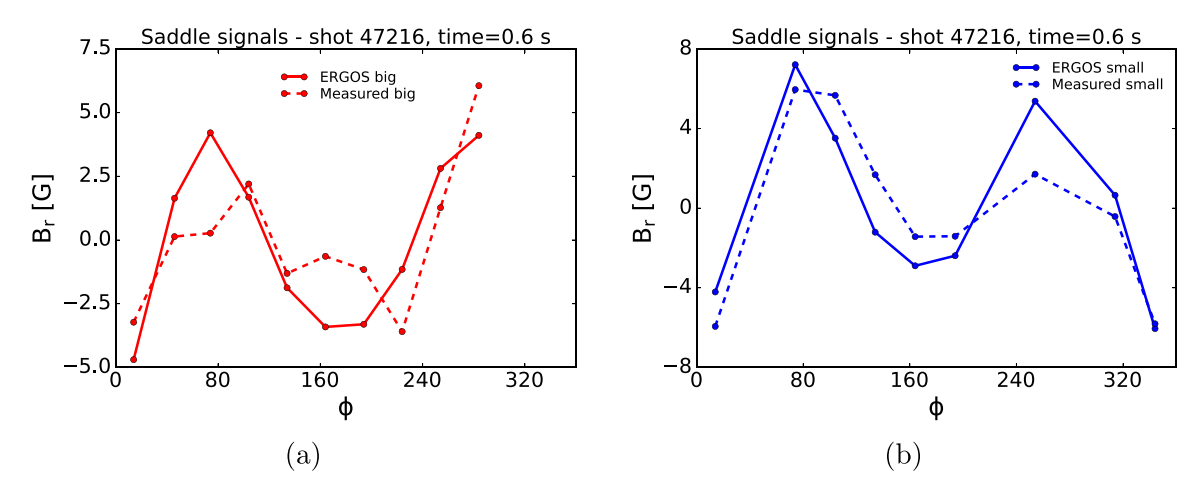
Previous MAST-U campaigns faced significant challenges in achieving ELM control. Multiple attempts were conducted using the external coils in the n = 2; however, none succeeded in reaching the threshold current necessary for ELM mitigation. Instead, in most cases, a LM was triggered, leading to early plasma termination. A possible explanation for these failures lies in the presence of a non-negligible n=2 EF, which could interfere with the externally induced perturbations. Indeed, in [10], a few experiments varying the absolute phase were reported, which confirmed the presence and the substantial effect of the n=2 EF. Historically, MAST-U has suffered from strong unwanted EFs originating from imperfections in the placement of poloidal field (PF) coils. The dominant EF contribution, in the n=1 configuration, has been successfully mitigated through mechanical adjustments, as confirmed by recent analyses [38]. However, no corrective measures have been implemented to address a potential n=2 component, as tilting or re-positioning the coils alone would not be effective. The failure of previous experiments motivates a detailed investigation and characterization of the n=2 EF. So far, only few discharges were performed while varying the relative phase in the n = 2 configuration. The results have been reported in table 1 in [10]; out of six shots, four of them resulted in a LM before achieving ELM mitigation while the other two did not have any effect at all. However, no full compass scan or any systematic experimental scan on the whole RMP parameters space have been performed yet. Moreover, to fully explain the modelocking dynamic, non-linear physics should be accounted for once the perturbed fields successfully penetrates. As such, the aim of this work is simply to quantify and characterize how the EF might modify the optimization of key metrics for ELM control. The focus, will lie on recomputing the optimal phases while incorporating a realistic, 3D EF plasma response model.

#### EF model

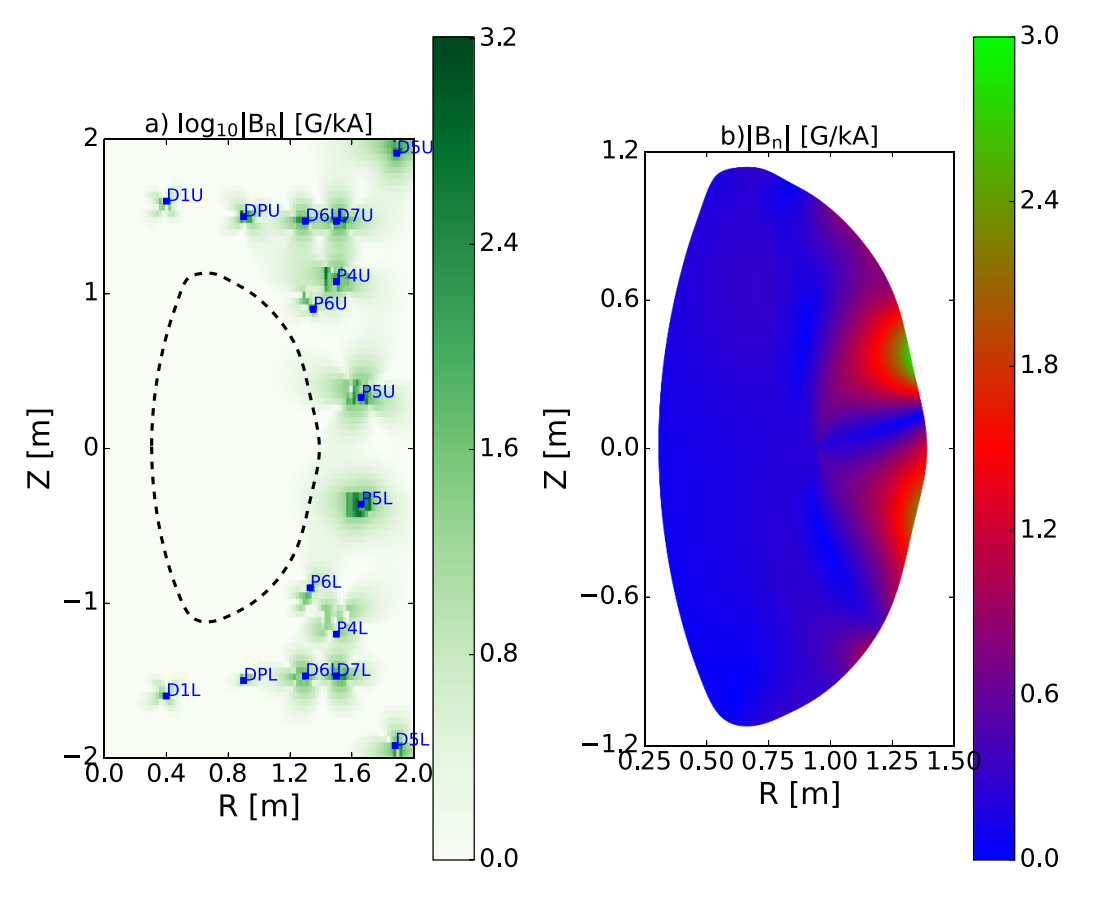
The EF model was derived by integrating vacuum discharge measurements into the fully toroidal Biot-Savart code, ERGOS [39], within which the detailed geometry of the MAST-U PF coil system has been inserted [40]. As a first check, to provide procedure validation, the model computations were compared to the experimental measurements obtained from the #47216 vacuum discharge during which only one set of PF coils, namely P5 (upper and lower) was powered. The P5 coil set was chosen since, as can be seen later in the discussion, its contribution to the EF turns out to be the predominant one. The measures were taken from the outboard saddles, a pair of toroidal arrays of saddle coils which, in MAST-U, allows to detect and evaluate the n > 0 component of the radial field  $B_R$ . The pair is divided into the big and the small saddles, which are positioned at the same radial location (around R = 1.99 m from the machine axis) with the center aligned with the machine's midplane. The coils have slightly different heights, hence the nomenclature, with the big spanning about 2 m and the small around 1.6 m. Being positioned right behind the P5, covering all their frames, these outboard saddles should detect the whole magnetic field produced by the poloidal coils, hence representing the best choice to compare vacuum discharges with the modeling results. It is worth noticing that the previous validation of the model was carried out in MAST which had worse capabilities in terms of radial field detection, instead, the comparison relied on measurements taken with three high-accuracy Hall probes that were installed ad-hoc [40].

Figure 10 shows the comparison between the saddles measurements and the ERGOS results taken at the same radius and at the toroidal angles  $\phi$  corresponding to the probes location. To best match the observations, ERGOS computations are also averaged over the nominal coils area. It should be noted that neither the *big* nor the *small* saddles cover entirely the toroidal circumference, instead they provide total coverage only when superposed. To obtain the EF measurement, the equilibrium contribution (i.e the mean value) to the radial field must be taken out from the signal. Then, when comparing the remaining n > 0 components with the correspondent ERGOS prediction, a satisfying match between model and measurements occurs. Notably, both the measured and the modeled signals display a clear n = 2 behavior.

A Fourier transform of the ERGOS 3D field was performed to correctly isolate the n=2 component. The computed vacuum field, for a unit current of 1 kAt, is shown in the left panel of figure 11. According to equations (5), to compute the plasma response using MARS-F, the EF must be translated into an equivalent current on a conformal surface outside the plasma boundary. This is achieved using the equivalent surface current (ESC) technique, which allows to prescribe an arbitrary magnetic field and to map it, by solving an inverse Biot–Savart problem, into the required input current [41]. This ensures that the plasma response calculation remains consistent within the entire domain enclosed by the ESC. The n=2 EF obtained via the ESC procedure was recomputed in MARS-F, and figure 12 shows the excellent



**Figure 10.** Comparison between the n > 0 radial field predicted by the ERGOS model (solid lines) and as detected from the outboard saddle probes (dotted lines) during discharge #47216, at 600 ms. Figure (a) shows the *big* saddle signals whereas (b) shows the *small* saddle signals. In both cases the ERGOS field has been obtained by averaging over the correspondent probe surface.



**Figure 11.** (a) n = 2 ERGOS  $B_R$  components (cylindrical coordinates) generated by the poloidal field coils (in blue) which distribution is marked in the poloidal section. The dashed line identifies the plasma boundary of #47051 at 611 ms. (b) n = 2 normal component of the ERGOS field interpolated on the MARS-F grid. The ERGOS field has been computed singularly for each poloidal coil reported in the left figure, assuming 1 kAt feeding current.

agreement between the vacuum field modeled by ERGOS and the results processed in MARS-F at the plasma boundary. The  $b_{\rm res}^1$  poloidal spectra of the computed EF, for both vacuum-only and with plasma response runs, is reported in figure 13. For comparison, figure 14 shows the spectra (obtained with plasma response) for the upper and lower rows of RMPs coils. By observing the maximum values of each spectra, it can be

immediately noted how the magnitude of the combined perturbation injected by the RMPs system, when in perfect constructive phase, would still be of the same order of the intrinsic EF.

To identify the primary sources of the n = 2 EF, computations were performed for each individual PF coil. Figure 15 indicates that the dominant contributions arise from the P4, P5,

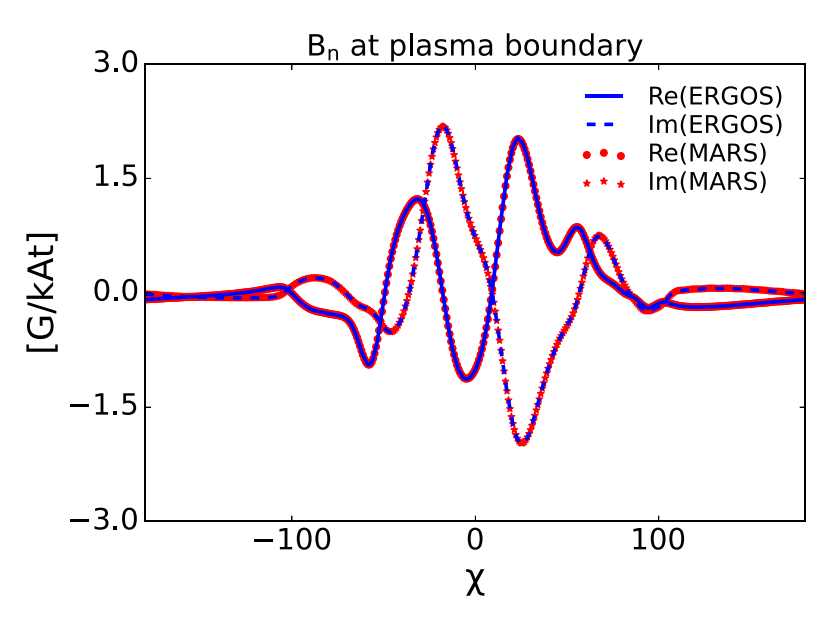


**Figure 12.** Poloidal distribution of the normal component of the n = 2 vacuum error field at the plasma boundary, computed assuming 1 kAt current flowing in the poloidal field system. Solid lines represent Re( $B_n$ ), whereas the dotted lines show Im( $B_n$ ). Blue color identifies the ERGOS field, while the red color shows the same field but computed in MARS-F after applying the ESC technique.

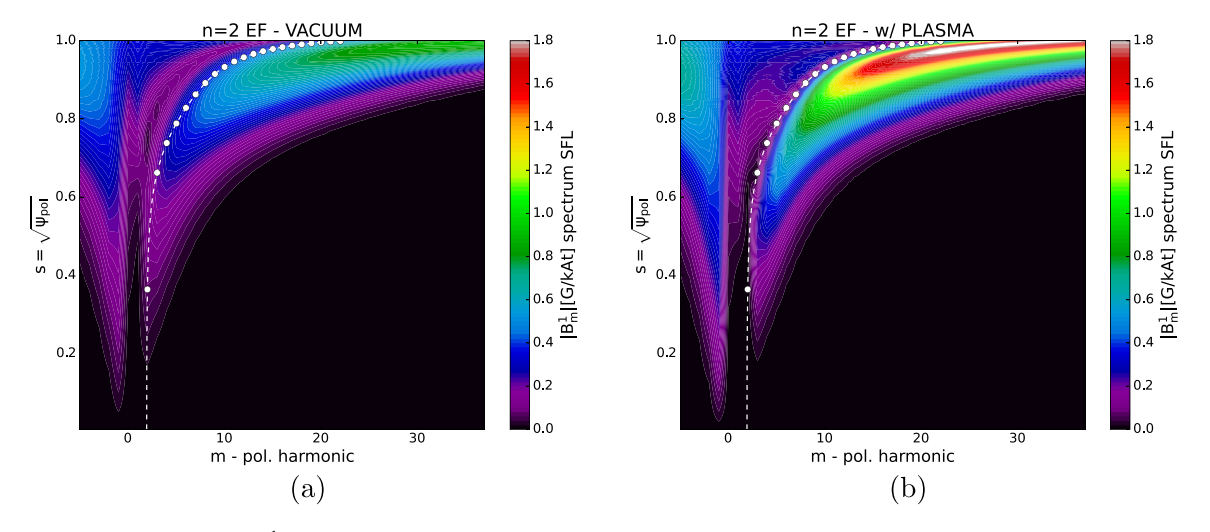


**Figure 13.** Poloidal spectrum of  $|b^1|$  per 1 kAt (in SFL coordinates) produced by the intrinsic n = 2 EF. (a) Vacuum field. (b) Total field (vacuum + plasma response). The dotted white line corresponds to the q profile while the white dots identify the positions of rational surfaces.

and P6 coil sets, with a minor contribution from the D coils. However, not all contributions are oriented in the same direction. The right panel of figure 15 illustrates the distribution of the perturbed radial field in the complex plane, in the radial location corresponding to the last resonant surface. While it shows partial cancellation between certain contributions like, for example, P4U and P4L, it also demonstrates that the overall largest contribution comes from the P5 coils, with the lower P5L coil being dominant. This analysis suggests that distancing the plasma column from the P5 coil set could help reduce the intrinsic EF. Furthermore, as shown in figures 15 and 16, the green bar/marker in the complex plane represents the perturbation induced by the ELM coil system when in maximum constructive phase. A direct comparison with the EF components confirms that both effects produce perturbations of the

same order of magnitude. This highlights the non-negligible impact of the intrinsic EF on the overall injected perturbation, potentially influencing the effectiveness of external RMP actuation.

To accurately assess the impact of EF-induced perturbations, the plasma response must account for the actual currents flowing in the PF coils during the experiment. In MAST-U, an external Rogowski coil is wrapped around each PF coil, enabling the precise estimation of the currents that feed the PF system [42]. For discharge #47051 at 611 ms, these currents are reported in table 1. Notably, the P5 coils, which already yield the strongest contribution, also appear to carry the largest fraction of the current. By re-scaling the ERGOS field with these experimentally measured currents, the actual effect of the EF plasma response during the discharge

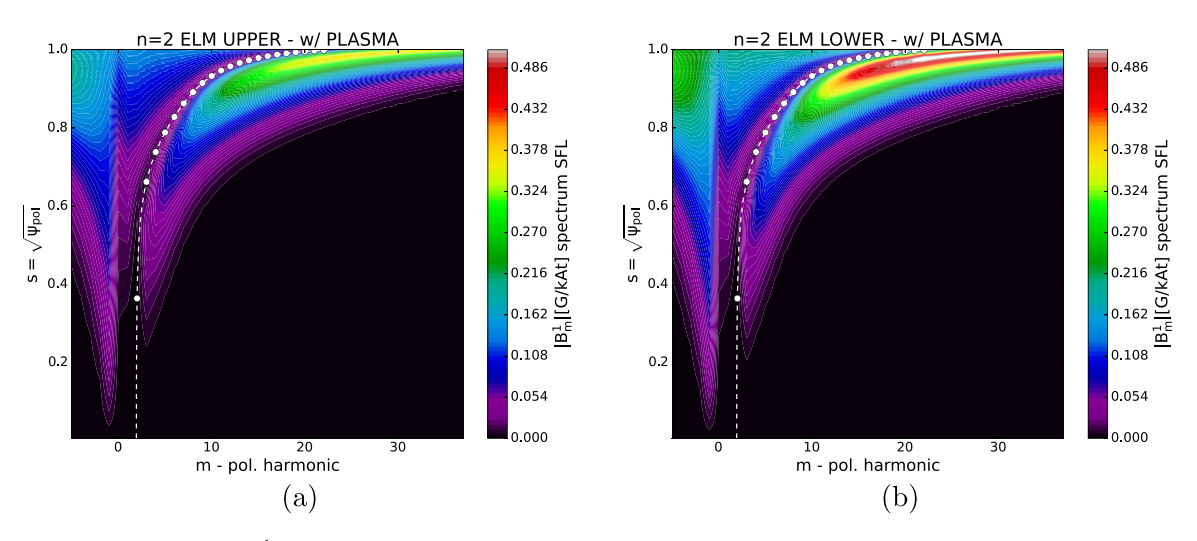


**Figure 14.** Poloidal spectrum of  $|b^1|$  (in SFL coordinates) total field produced by the ELM coil sets in n = 2 configuration, assuming an input current perturbation of 1 kAt. (a) ELM coils, upper row. (b) ELM coils, lower row. The dotted white line corresponds to the q profile while the white dots identify the positions of rational surfaces.



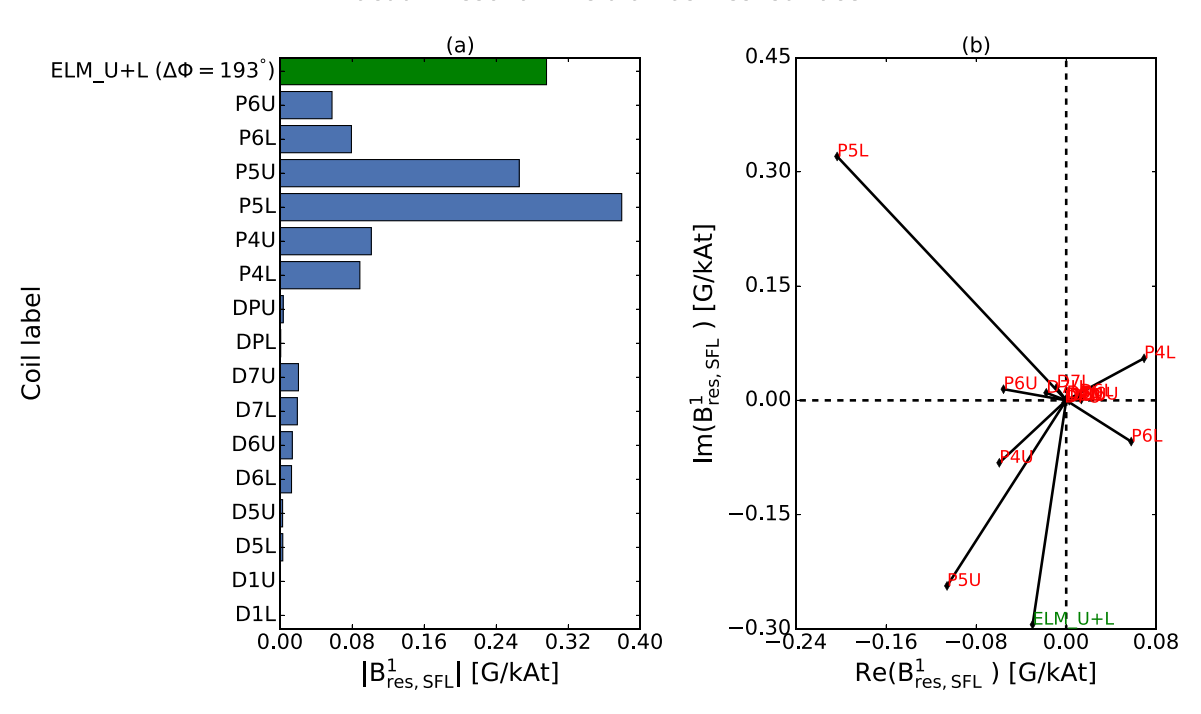


**Figure 15.**  $b^1$  resonant component (in SFL coordinate) of the vacuum n=2 EF and RMP perturbations computed at the q=11 rational surface. (a) Histogram bars representing the absolute value of the field for each individual error field source. The green bar shows the absolute values correspondent to the sum of the ELM upper and lower row at the maximum alignment phase. (b) Representation of the field in the complex plane. Opposite vectors are in phase-opposition hence they would destructively add up. The  $b^1$  field is computed assuming 1 kAt current flowing in each coil.

can be determined. Those re-scaled computations, shown in figure 16, confirm the P5 coils as the dominant sources of EF. Furthermore, the actual perturbation amplitude, due to the EF alone, measures up to  $\sim$  3G, representing a substantial effect.

# EF correction (EFC) to the metrics

By linearly combining the plasma response to the n=2 EF with the perturbation generated by the ELM control coils, the

effect of the EF on key optimization metrics can be evaluated. Figure 17 shows the phase scan of both the linear metrics with the EF included compared to the curves obtained without. From the left panel, it is possible to appreciate the shift of the resonant field metrics. Notice that, since the regular behavior displayed by the different polodial harmonics for the n=2 case (figure 4(b)), here for simplicity only the resonant field at the last-pitch aligned surface has been reported. When including the EF, the vacuum and the total optimal

# Vacuum resonant field at last res. surface. Experimental coils currents

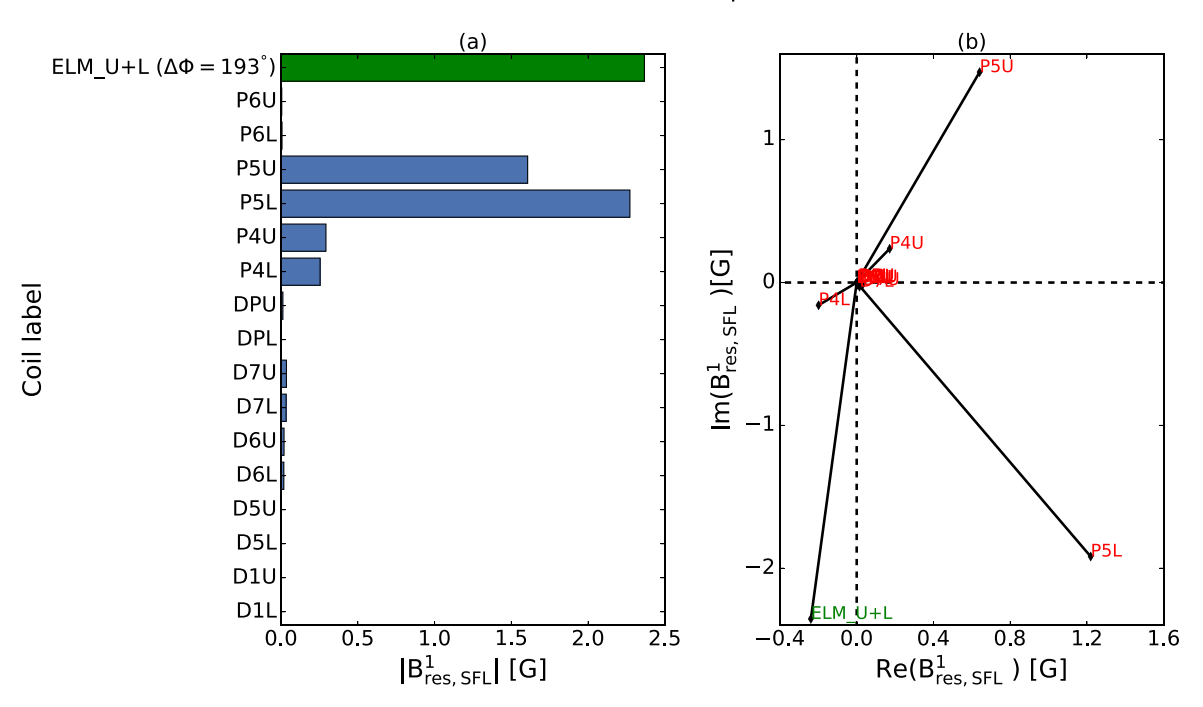


Figure 16. Same as figure 15 but here the  $b^1$  field is scaled with the experimental value of the source currents, taken at 611 ms for the discharge #47051, in each poloidal field coil. The RMP field is scaled with the maximum nominal current: 8 kAt.

**Table 1.** Values of the currents feeding each PF coil (both Upper and Lower) during shot #47051 at 611 ms (in kAt), as measured by the external Rogowsky coil. P5 information are highlighted.

P4	P5	P6	D1	D5	D6	D7	DP
	-6.05 $-5.99$						

alignments get moved behind of  $\sim 50^{\circ}$  and  $\sim 70^{\circ}$  respectively. The displacement ratio metric (right panel) displays, instead, a more drastic shift. The new optimum is shifted, for both the X-points, close to almost 0° relative phasing and the ratio drops marginally above one for  $\xi_U$  and even below for  $\xi_L$ . A displacement ratio smaller than the unity indicates that the kink-like response is dominating hence affecting, potentially in a detrimental way, the core confinement. This interpretation may be further supported, at least qualitatively, by the limited set of experimental data points available in table 1 of [10]. The corresponding values of the relative phase  $\Delta \Phi$ , associated with either the onset of a LM (crosses) or a lack of effects (circles), have been overlaid in figure 17(b). It can be observed that the inclusion of the intrinsic EF tends to shift the displacement ratio  $\xi_X/\xi_M$  toward values less than unity in the phase intervals where LMs are experimentally observed. This suggests that, if unfavorably aligned with the EF, the perturbations may effectively lead to core braking and mode locking. The only clear deviation from this trend is represented by the rightmost cross. Again, it should be noted that a fully quantitative explanation of the LM onset requires a non-linear treatment of the plasma response, which is beyond the scope of this analysis. Moreover, small differences between the equilibrium and kinetic profiles used in the modelling and those corresponding to the actual experimental discharges could also contribute to explaining the discrepancy. To investigate a little more in detail the influence of the EF, the evolution of the metric optimization is shown as the RMP current is rampedup from 1 to 8 kAt, which is the maximal nominal current of the coil set (figure 18). Initially, the EF dominates the field response, shifting the optimization to  $\sim 131^{\circ}$ . However, as  $I_{\rm RMP}$  increases, the intrinsic field is gradually compensated by the ELM coils which attempt to restore the original optimum. Indeed, once the current finally saturates, the predicted shift settles down at  $\sim 160^{\circ}$ . The optimal curve for the same metric but for the case without EF is also shown (black-dashed in the figure) for comparison sake. Aside from shifting the optimum, the inclusion of the EF also induces extra magnitude to the radial field which increases by approximately 30%.

When looking at the displacements metric, instead, the changes in the ratio values can be explained by observing figure 19 which shows the  $\Delta \Phi$  dependence of the absolute value of  $\xi$  in each region considered. When adding the EF all the displacements are increased and shifted of few degrees. In particular, the displacement at the midplane becomes the dominant one and, most importantly, the maximum of each curve

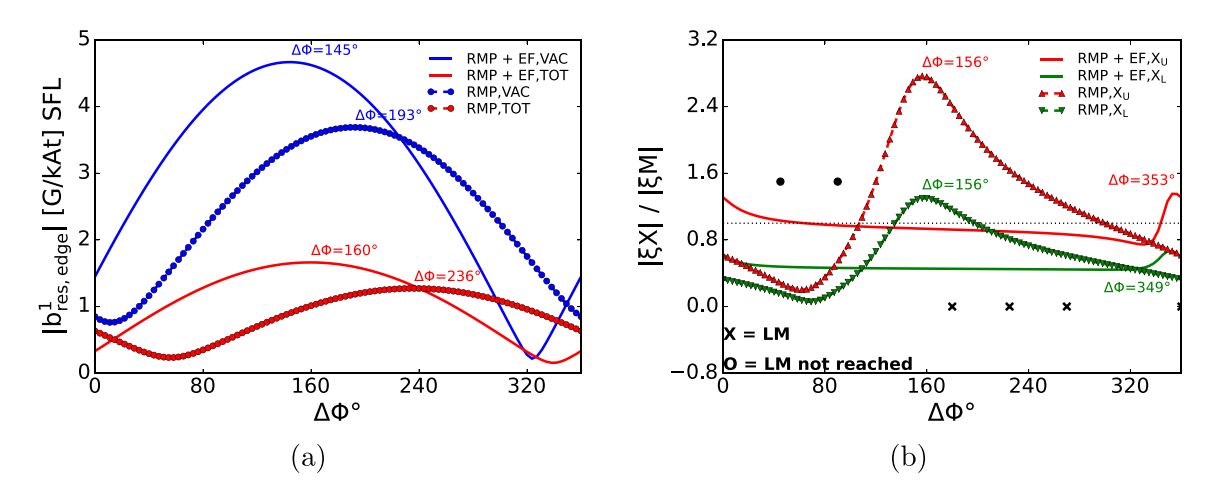


Figure 17.  $\Delta\Phi$  scan of the linear, fluid metrics adding the EF effect. *Left*:  $|b_{\rm res}^1|$  metric. Here blue is the vacuum field while red is the total one. *Right*:  $\xi_L/\xi_M$  metric. The green curves corresponds to  $\xi_L$ , while the red one to  $\xi_U$ . The dotted lines correspond to the case without EF and with the RMP system at full power (8 kAt). The solid lines are obtained by summing the EF. In the left figure (*b*), also the experimental points from table 1 in [10] have been reported. Here crosses identify  $\Delta\Phi$  for which locked modes were triggered while circles corresponds to alignments without LMs.

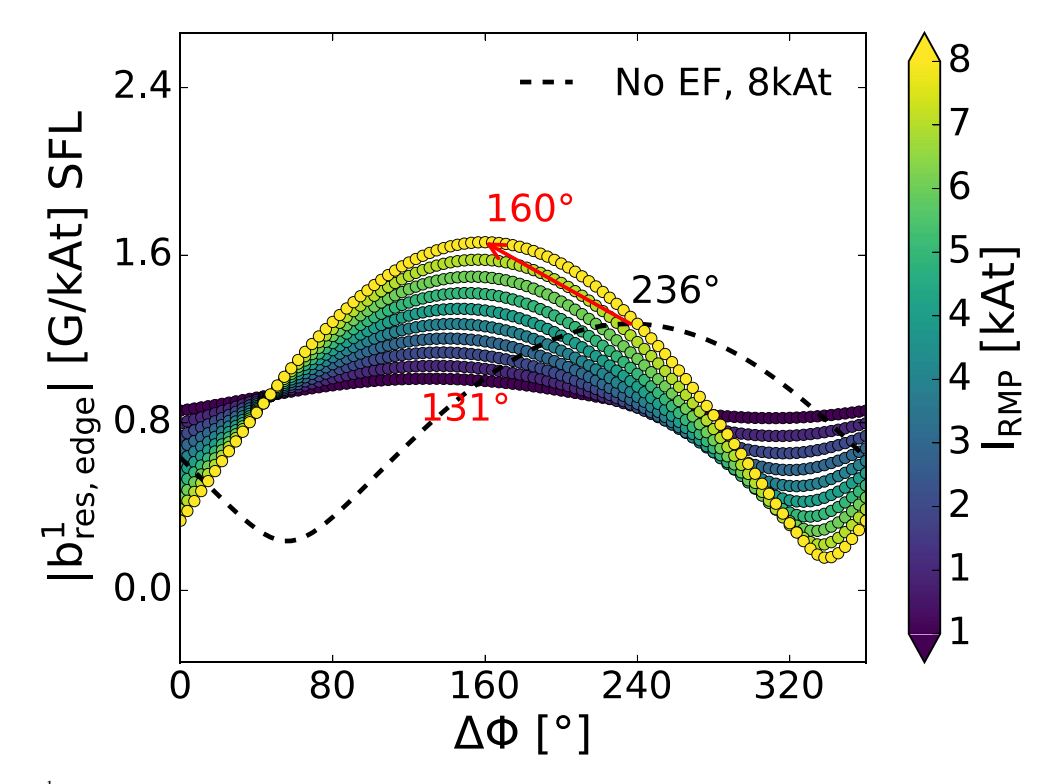
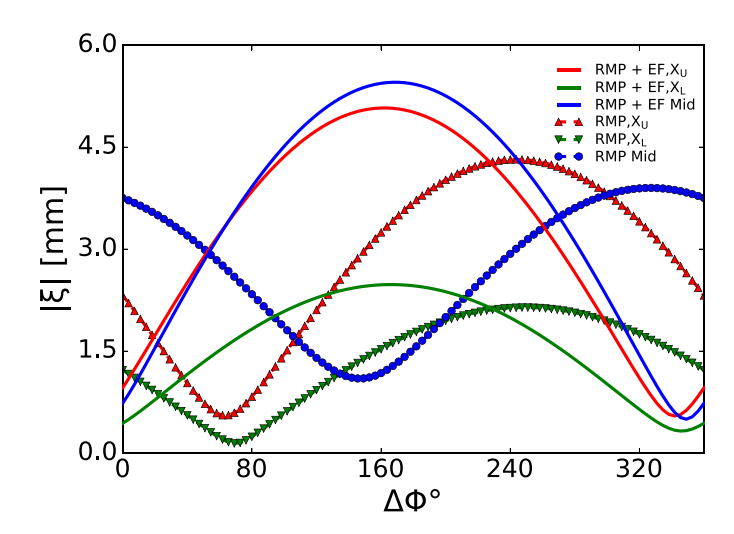


Figure 18. Total  $|b_{\text{res,edge}}^1|$  field metric for the case RMP + EF varying the RMP current from 1 kAt (blue-ish) to 8 kAt (yellow-ish), while fixing the latter. The black dashed curve shows the optimum trend for the total  $|b_{\text{res,edge}}^1|$  field, at 8 kAt, without the EF.

aligns at the same relative phase. This strongly suggest that the EF would dominate the response, non-negligibly affecting the core.

The analysis of the torque ratio metric further consolidate previous observations. Figure 20 shows  $\tau_{\rm edge}/\tau_{\rm core}$  while varying  $\Delta \Phi$  and scanning simultaneously the current amplitude ratio, fixing  $I_U=8$  kAt. Clearly, when adding the EF, the relative coil current amplitude looses importance in determining the optimal configuration. In fact, the maximum ratio is

obtained when both the rows of coils are activated at full current. Moreover, while the torque ratio remains overall above the unity, its magnitude gets sensibly reduced, to a maximum of 3 (figure 6(a)). The relative phase dependence is also inverted, with the optimum now localized around  $0^{\circ}$ , in line with the displacement ratio metric prediction, and a region of core torque dominance is found for the combination of parameters:  $I_L \in [0.3, 0.8] * I_U$  and  $\Delta \Phi \in [260^{\circ}, 320^{\circ}]$ . In general, both the core and the edge regions seem to be braked with a similar



**Figure 19.** Magnitude of the displacements  $\xi$  measured at midplane (blue) and at both the X-points ( $\xi_U$ ,  $\xi_L$ ). The dotted lines correspond to the case without EF and RMPs at full power.

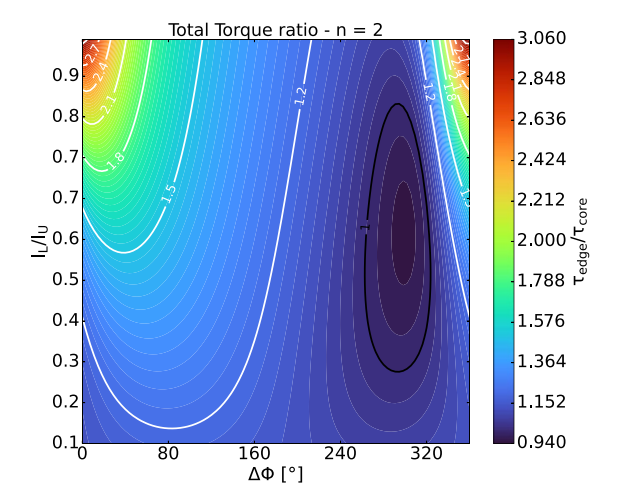
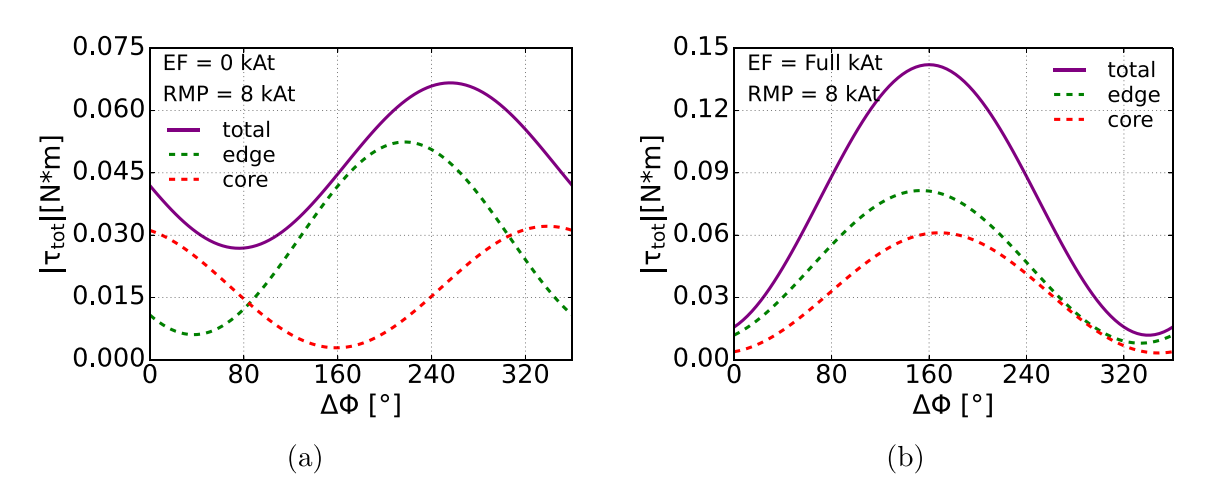


Figure 20.  $\tau_{\rm edge}/\tau_{\rm core}$  metric computed adding the effect of the EF. Here the current amplitude ratio is computed by fixing  $I_U = 8 {\rm kAt}$  and varying  $I_L$ .



**Figure 21.** Integrated torque magnitudes, in absolute values, varying  $\Delta \Phi$ . Different spatial regions are denoted by colors with: red the core region, green the edge and purple the whole radius. (a) Torque injected by powering the RMP coils at full current (8 kAt). (b) torque injected by powering the RMP coils at full regime and including the EF scaled with the experimental currents.

magnitude now and the introduction of the EF clearly causes the disruption of the decoupling which was achieved by the ELM control coils alone (figures 21(a) and (b)). This result points again in the direction of EF to be mostly affecting the core region of the plasma column. Notably, due to the presence of the EF, the core induced torque is now maximized at the RMPs-only optimal phase, assuming a peak value of  $\tau_{\rm tot}\sim 140$  mNm and  $\tau_{\rm core}\sim 60$  mNm which would be the double of the core torque induced by the RMP coils alone, even when aligned with an unfavorable phasing. This could provide an explanation for the observations of LMs when the RMP coils were set to the predicted optimum without accounting for the EF presence.

#### 5. Conclusions

This study investigated the role of linear and quasi-linear modeling to understand, and eventually achieve, ELM control in the spherical tokamak MAST-U. Particular focus has been set on the correlation between the plasma response to external RMPs and the presence of an intrinsic EF. In terms of optimization, this work evaluated the relative effectiveness of fluid and kinetic metrics in guiding ELM mitigation strategies. While, in general, validation with the experiments is essential to clarify which figure of merit should be applied, some considerations can be done about the reliability and the convenience for the use of each metric. The resonant radial field is usually a robust metric which value mostly relies on predicting whether the system is able, or not, to produce enough perturbation to affect the plasma and achieve control. This metric usually display broad peaks around the optimal configuration points and it can also quantify the plasma response shift throughout different resonant surfaces. However, to be applied in a recipe the results computed with this metric necessarily requires comparison with the experiment and it is usually device-dependent. It can, in turn, represent the fastest way to determine the optimal coil parameters when ELMs control has already been achieved on a device. In order to better understand the details of the response to the perturbation, the radial field metric should be complemented by a figure of merit that decouples the types of response, this could also be useful to prevent the on-set of dangerous locked-modes while still investigating the coilset parameter space. The displacement-based metric displays a strong optimum localization feature. While notable results have been previously achieved using this metric, it remains device-dependent and it may turn out to be unreliable if the scenario characteristics happen to be too uncertain. The torque ratio metric, which accounts for the mutual coupling between each set of coils (and EF) show a remarkable agreement with the displacement metric, this result further consolidate the validity of the latter despite its linear nature. The usefulness of this metric could be found into assessing the safety region of coil configurations prior to experimentation. However, simply having a torque ratio slightly above the unity could be not enough to prevent detrimental effects in the core region and, in general, assessments on the overall torque magnitude should always be performed. Analysis of the composition of the fluid torque on MAST-U identifies the dominant role of the  $\mathbf{j} \times \mathbf{b}$  process which requires minimization in the core and maximization at the edge. So far only the optimal  $\Delta \Phi$  an  $I_L/I_U$  ratio have been computed with the fluid quasi-linear torque metric which, in principle, could also be used to derive the minimum current magnitude to achieve penetration by evolving the single-fluid momentum equation using the RMP torque as input source. This is currently left as future work.

The quasi-linear kinetic analysis, even if still unrefined, provided a good comparison with the more traditional resonant field metric and an adequate agreement in the prediction of the optimal phase is demonstrated between the two workflows. A precise assessment of the RMPs magnitude needed to achieve the full penetration, even if time consuming, helps in determining the validity threshold for the linear metrics. In future, comparing penetration dynamic as computed in the kinetic and fluid models would further deepen the physical understanding of RMPs applied to the ELM control. This pushes in the direction of directly benchmark the two quasi-linear frameworks. Moreover, careful analysis of the dependency on other kinetic parameters should be carried out to improve the characterization of the metric sensitivity and enhance the modeling prediction capability.

In general, all these findings suggest that careful consideration of metric selection is essential to develop effective ELM control strategies in MAST-U.

Finally, this analysis characterized and quantified the dominant contribution to the n=2 component of the intrinsic EF associated with the PF system. The plasma response computations indicate that the EF may affect non-negligibly the core region, possibly compromising confinement and preventing ELM mitigation. Unfortunately, to mechanically correct the imperfections that produce all the unwanted n > 1 components is not practically feasible, as it would require bending and deforming the coils shape, hence likely incurring in the risk of breaking them. Operation-wise, it could be a solution to try to adjust the plasma column to distance it from the P5 coil set. Alternatively, a possibility could be implementing EFC with another set of external 3D coils such as the EFC coils which have been previously applied to correct the n = 1EF [11]. In the meanwhile, in this work alternative optimal phases have been computed including the model-based presence of the EF. Nevertheless, a thorough investigation should also include potential contributions from the toroidal field system and central solenoid to ensure a comprehensive evaluation of the intrinsic fields. This is, again, left as future work.

# Acknowledgment

We thank Dr L. Piron and her student M. Gambrioli for the useful discussions about the error field presence in MAST-U. This work has been carried out within the framework of the EUROfusion Consortium, funded by the European Union via the Euratom Research and Training Programme (Grant Agreement No. 101052200 - EUROfusion) and from the EPSRC (Grant Number EP/W006839/1). Views and opinions expressed are however those of the author(s) only and

do not necessarily reflect those of the European Union or the European Commission. Neither the European Union nor the European Commission can be held responsible for them.

# Appendix. MARS-F shielding current integration

Bridging between MARS-F and the KilCA code requires the computation of the parallel component of the perturbed current density  $\mathbf{j}_{//}$  which arise in response to any external magnetic perturbation. This can be done directly starting from MARS-F outputs. Indeed:

$$\mathbf{j}_{\parallel} = \frac{\mathbf{j} \cdot \mathbf{B}_0}{B_0} \tag{A.1}$$

where  $\mathbf{B}_0$  is the equilibrium field and  $B_0$  its modulus. This expression can be expanded in terms of MARS-F variables since  $B_0 = [B_0^1, B_0^2, B_0^3] = [0, \psi'/J, F/R^2]$  with  $\psi' = \mathrm{d}\psi/\mathrm{d}s$  and with  $\psi$  being the poloidal flux, J the metric Jacobian and F the poloidal current flux function and where 1,2,3 superscripts denominates the radial, poloidal and toroidal components respectively. Then:

$$j^{i}B_{i} = \frac{j^{1}\psi'g_{12}}{I} + \frac{j^{2}\psi'g_{22}}{I} + j^{3}F$$
 (A.2)

$$B_0 = |\mathbf{B}_0| = \sqrt{B_0^i B_{i,0}} = \sqrt{0 + \psi' g_{22}/J^2 + (F/R)^2}$$
 (A.3)

with  $g_{ij}$  being the metric elements. Finally:

$$j_{\parallel}^{\text{MARS}-F} = \frac{j^{1}\psi'g_{12}/J + j^{2}\psi'g_{22}/J + j^{3}F}{\sqrt{\psi'g_{22} + (F/R)^{2}}}.$$
 (A.4)

The parallel current density determined in real space with MARS-F is expanded for Boozer coordinates in Fourier harmonics. For a single harmonic, we have

$$\mathbf{j}_{\parallel} = \mathbf{B_0} \left( \frac{\mathbf{j}_{\parallel}}{B_0} \right)_{\mathbf{m}} e^{\mathrm{i}\vartheta_B m + \mathrm{i}\varphi_B n},$$
 (A.5)

where  $(j_{\parallel}/B_0)_{\mathbf{m}}$  is the Boozer harmonic of the current in toroidal geometry for the specific mode number  $\mathbf{m}=(m,n)$ . Note that the current calculated by MARS-F is given for a specific toroidal mode in geometrical angles. Hence, we need to account for a phase factor occurring in the transformation to the toroidal Boozer angle

$$j_{\parallel,n}\left(s_{p},\vartheta_{B}\right)=j_{\parallel,n_{g}}^{\text{MARS-F}}\left(s_{p},\vartheta_{g}\left(\vartheta_{B}\right)\right)e^{-inG\left(s_{p},\vartheta_{B}\right)},\qquad(A.6)$$

where  $n_g$  indicates the toroidal mode number for the geometrical angle used in MARS-F.

To get the mode specific parallel current, we integrate over a surface S,

$$I_{\parallel \mathbf{m}} = \int d\mathbf{S} \cdot \mathbf{B}_0 \left( \frac{j_{\parallel}}{B_0} \right)_{\mathbf{m}}.$$
 (A.7)

We choose the surface to be a toroidal surface, i.e. fixed toroidal angle, meaning that  $d\mathbf{S}_{tor} \cdot \mathbf{B}_0 = d\Psi_{tor}$ . Hence,

$$I_{\parallel \mathbf{m}} = \int \mathrm{d}\Psi_{\mathrm{tor}} \left(\frac{j_{\parallel}}{B_0}\right)_{\mathbf{m}}.$$
 (A.8)

To proceed we realize that, in the case of flux variables, the harmonic of the current density only depends on  $s=\sqrt{\Psi_{\rm pol}^n}$ , where  $\Psi_{\rm pol}^n$  is the normalized poloidal flux, or  $\Psi_{\rm pol}=\Psi_{\rm pol}^as^2$  with the poloidal flux at the last closed flux surface,  $\Psi_{\rm pol}^a$ . We further recall that the safety factor is defined as

$$q = \frac{\mathrm{d}\Psi_{\mathrm{tor}}}{\mathrm{d}\Psi_{\mathrm{pol}}}.\tag{A.9}$$

With this, we can write  $d\Psi_{tor} = 2\Psi_{pol}^{a}sds$ , with which the integration is written as

$$I_{\parallel \mathbf{m}} = 2\Psi_{\text{pol}}^{a} \int_{s_{\text{res}} + s_{\text{d}}}^{s_{\text{res}} + s_{\text{d}}} \mathrm{d}s \, sq \left(\frac{j_{\parallel}}{B_{0}}\right)_{\mathbf{m}}.\tag{A.10}$$

Note that the integration is over a region around the resonant surface with  $s_{res}$ . Previously [14], the width of this region was determined by a Gaussian fit, where  $s_d$  was taken to be five times the standard deviation. Here, however, it proved more consistent to integrate between the two neighbouring minima around a resonant surface.

### **ORCID iDs**

E. Tomasina © 0009-0004-0385-9491
M.J. Markl © 0009-0005-7283-1668
L. Pigatto © 0000-0002-0556-0440
D. Ryan © 0000-0002-7735-3598
C.G. Albert © 0000-0003-4773-416X
E. Viezzer © 0000-0001-6419-6848
Y.Q. Liu © 0000-0002-8192-8411
T. Bolzonella © 0000-0003-1128-964X

#### References

- [1] Zohm H. 1996 Plasma Phys. Control. Fusion 38 1213-23
- [2] Loarte A., Campbell D., Gribov Y., Pitts R., Klimov N., Podkovyrov V., Zhitlukhin A., Landman I., Pestchanyi S. and Bazylev B. 2010 IAEA Fusion Energy Conf. Book of Abstracts
- [3] Lang P. et al (the ASDEX Upgrade Team) 2004 Nucl. Fusion 44 665
- [4] Evans T. et al 2005 J. Nucl. Mater. 337-339 691-6
- [5] Kirk A., Chapman I.T., Harrison J., Liu Y., Nardon E., Saarelma S., Scannell R. and Thornton A.J. (the MAST Team) 2012 Plasma Phys. Control. Fusion 55 015006
- [6] Kirk A. *et al* (the MAST Upgrade Team and the ASDEX Upgrade Team) 2015 *Nucl. Fusion* **55** 043011
- [7] Evans T. et al 2008 Nucl. Fusion 48 024002
- [8] Kirk A., Liu Y., Chapman I.T., Harrison J., Nardon E., Scannell R. and Thornton A.J. (the MAST Team) 2013 Plasma Phys. Control. Fusion 55 045007
- [9] Kirk A. et al 2010 Nucl. Fusion 50 034008
- [10] Ryan D.A. et al 2024 Plasma Phys. Control. Fusion 66 105003

[11] Piron L., Kirk A., Liu Y.Q., Cunningham G., Carr M., Gowland R., Katramados I. and Martin R. 2020 Fusion Eng. Des. 161 111932

- [12] Shafer M.W., Paz-Soldan C., Evans T.E., Lyons B.C., Osborne T.H. and Turnbull A.D. 2020 28th IAEA Fusion Energy Conf. (FEC), (London) IAEA-EX-P1/930 (available at: https://nucleus.iaea.org/sites/fusionportal/Shared%20 Documents/FEC%202020/fec2020-preprints/preprint0930. pdf)
- [13] Liu Y., Kirk A. and Nardon E. 2010 *Phys. Plasmas* 17 122502
- [14] Markl M., Ulbl P., Albert C.G., Angioni C., Buchholz R., Heyn M.F., Kasilov S.V., Kernbichler W., Suttrop W. and Willensdorfer M. 2023 Nucl. Fusion 63 126007
- [15] Ltitjens H., Bondeson A. and Sauter O. 1996 Comput. Phys. Commun. 97 219–60
- [16] Appel L. and Lupelli I. 2018 *Comput. Phys. Commun.* **223** 1–17
- [17] Kogan L. et al (MAST Upgrade Team) 2022 48th EPS Conf. on Plasma Physics (27 June–1 July 2022) (European Physical Society (EPS)) (available at: https://research.tue. nl/files/274268100/P2a.116.pdf)
- [18] Ryan D.A., Liu Y.Q., Li L., Kirk A., Dunne M., Dudson B., Piovesan P., Suttrop W. and Willensdorfer M. 2017 Plasma Phys. Control. Fusion 59 024005
- [19] Bondeson A. and Iacono R. 1989 Phys. Fluids B 1 1431-43
- [20] Bondeson A., Liu Y. and Fransson C.M. 2002 Nucl. Fusion 42 768
- [21] Fitzpatrick R. 2012 Plasma Phys. Control. Fusion 54 094002
- [22] Ivanov I.B., Heyn M.F., Kasilov S.V. and Kernbichler W. 2011 Phys. Plasmas 18 022501
- [23] Martitsch A.F. et al (The ASDEX Upgrade Team and the EUROfusion MST1 Team) 2016 Plasma Phys. Control. Fusion 58 074007
- [24] Valovič M. *et al* (The MAST Team) 2005 *Nucl. Fusion* **45** 942–9

- [25] Heyn M.F., Ivanov I.B., Kasilov S.V., Kernbichler W., Leitner P., Nemov V.V. and Suttrop W. (the ASDEX Upgrade Team) 2014 Nucl. Fusion 54 064005
- [26] Park J.-K., Boozer A. and Glasser A. 2007 *Phys. Plasmas* **14** 052110
- [27] Park J.K., Boozer A.H., Menard J.E., Garofalo A.M., Schaffer M.J., Hawryluk R.J., Kaye S.M., Gerhardt S.P. and Sabbagh S.A. 2009 Phys. Plasmas 16 082512
- [28] Park J.-K. and Logan N.C. 2017 Phys. Plasmas 24 032505
- [29] Liu Y., Ham C.J., Kirk A., Li L., Loarte A., Ryan D.A., Sun Y., Suttrop W., Yang X. and Zhou L. 2016 Plasma Phys. Control. Fusion 58 114005
- [30] Suttrop W. et al 2018 Nucl. Fusion 58 096031
- [31] Park J.-K. et al 2018 Nat. Phys. 14 1223-8
- [32] Li L., Liu Y.Q., Loarte A., Pinches S.D., Polevoi A. and Zhong F.C. 2020 Phys. Plasmas 27 042510
- [33] Shaing K.C., Sabbagh S.A. and Chu M.S. 2010 Nucl. Fusion 50 025022
- [34] Sun Y., Liang Y., Shaing K.C., Koslowski H.R., Wiegmann C. and Zhang T. 2011 Nucl. Fusion 51 053015
- [35] Wang Z., Park J.K., Liu Y., Logan N., Kim K. and Menard J.E. 2014 Phys. Plasmas 21 042502
- [36] Yang X., Liu Y., Sun Y., Wang H., Gu S., Jia M., Li L., Liu Y., Wang Z. and Zhou L. 2018 Plasma Phys. Control. Fusion 60 055004
- [37] Nazikian R. et al 2015 Phys. Rev. Lett. 114 105002
- [38] Gambrioli M., Piron L., Cunningham G., Terranova D., Baruzzo M., Joffrin E., Labit B., Martin P., Ryan D. and Vincent C. 2024 *Fusion Eng. Des.* 205 114544
- [39] Bécoulet M. et al 2008 Nucl. Fusion 48 024003
- [40] Kirk A., Liu Y., Martin R., Cunningham G. and Howell D. 2014 Plasma Phys. Control. Fusion 56 104003
- [41] Yueqiang Liu A. and Kirk A.J.T. (The MAST Team) 2014 Plasma Phys. Control. Fusion 56 104002
- [42] Ryan D.A., Martin R., Appel L., Ayed N.B., Kogan L. and Kirk A. 2023 Rev. Sci. Instrum. 94 073501